

# Wind Turbulence over Misaligned Surface Waves and Air–Sea Momentum Flux. Part I: Waves Following and Opposing Wind

NYLA T. HUSAIN,<sup>a</sup> TETSU HARA,<sup>a</sup> AND PETER P. SULLIVAN<sup>b</sup>

<sup>a</sup> *Graduate School of Oceanography, University of Rhode Island, Narragansett, Rhode Island*

<sup>b</sup> *National Center for Atmospheric Research, Boulder, Colorado*

(Manuscript received 25 February 2021, in final form 8 November 2021)

**ABSTRACT:** Air–sea momentum and scalar fluxes are strongly influenced by the coupling dynamics between turbulent winds and a spectrum of waves. Because direct field observations are difficult, particularly in high winds, many modeling and laboratory studies have aimed to elucidate the impacts of the sea state and other surface wave features on momentum and energy fluxes between wind and waves as well as on the mean wind profile and drag coefficient. Opposing wind is common under transient winds, for example, under tropical cyclones, but few studies have examined its impacts on air–sea fluxes. In this study, we employ a large-eddy simulation for wind blowing over steep sinusoidal waves of varying phase speeds, both following and opposing wind, to investigate impacts on the mean wind profile, drag coefficient, and wave growth/decay rates. The airflow dynamics and impacts rapidly change as the wave age increases for waves following wind. However, there is a rather smooth transition from the slowest waves following wind to the fastest waves opposing wind, with gradual enhancement of a flow perturbation identified by a strong vorticity layer detached from the crest despite the absence of apparent airflow separation. The vorticity layer appears to increase the effective surface roughness and wave form drag (wave attenuation rate) substantially for faster waves opposing wind.

**SIGNIFICANCE STATEMENT:** Surface waves increase friction at the sea surface and modify how wind forces upper-ocean currents and turbulence. Therefore, it is important to include effects of different wave conditions in weather and climate forecasts. We aim to inform more accurate forecasts by investigating wind blowing over waves propagating in the opposite direction using large-eddy simulation. We find that when waves oppose wind, they decay as expected, but also increase the surface friction much more drastically than when waves follow wind. This finding has important implications for how waves opposing wind are represented as a source of surface friction in forecast models.

**KEYWORDS:** Wind stress; Wind waves; Air–sea interaction; Large eddy simulations

## 1. Introduction

There is a continued interest in improving the prediction and parameterization of momentum, energy, heat, and gas exchanges between the ocean and atmosphere. It is well known that the coupling between wind and ocean surface waves modifies turbulent air–sea fluxes, thereby playing a substantial role in the development of weather and climate patterns forecast by numerical models (Cronin et al. 2019). Yet, many uncertainties remain as to how wind–wave coupling impacts air–sea momentum and scalar fluxes, as well as wave growth and dissipation, under a range of sea states (Sullivan and McWilliams 2010).

Coupled ocean, atmosphere, and wave models often struggle to accurately forecast the evolution of wave fields, ocean currents, storm surge, and weather events without accounting for the effects of wind–waves and swell on the wind stress or drag coefficient  $C_d$  (Moon et al. 2003, 2004, 2009; Fan et al. 2009; Donelan et al. 2012; Reichl et al. 2014; Cronin et al. 2019). Most existing models rely on an empirically derived bulk  $C_d$  that uses Monin–Obukhov similarity relationships to define the wind stress as a simple function of wind speed in neutral conditions (e.g., Large and Pond 1981; Edson and

Fairall 1998). To account for the wave effects (sea state) in a relatively simple manner, many studies have addressed the impacts of wave parameters such as wave age ( $c/u_{*s}$ , where  $c$  is the wave phase speed and  $u_{*s}$  is the wind friction velocity) and wave steepness ( $ak$ , where  $a$  is the wave amplitude and  $k$  is the wavenumber) on the wind stress and sea surface roughness (Banner and Melville 1976; Banner 1990; Belcher et al. 1993; Donelan et al. 1993; Makin and Kudryavtsev 1999; Fairall et al. 2003; Edson et al. 2013).

A number of more complex models and parameterizations have been developed to account for the effects of wave-driven turbulent processes near the wavy surface under strong wind forcing. Such processes include airflow separation over breaking waves (Kudryavtsev and Makin 2001; Makin and Kudryavtsev 2002; Donelan et al. 2006; Mueller and Veron 2009; Kukulka et al. 2007; Kukulka and Hara 2008; Suzuki et al. 2013), ejection of sea spray and spume from wave crests (Andreas 2004; Kudryavtsev and Makin 2011; Richter and Sullivan 2013; Veron 2015), enhanced bubble production, air entrainment and gas transfer by breaking waves (Deike et al. 2017; Deike and Melville 2018), and near-surface ocean currents driven by waves (Teixeira 2018; Wang et al. 2019), to name a few. A variety of parameterizations have also been developed to represent the effects of wind–wave misalignment on wave growth and dissipation (e.g., Tolman and Chalikov 1996; Meirink et al. 2003; Kudryavtsev and Makin 2004;

Corresponding author: Nyla T. Husain, nylahusain@uri.edu

DOI: 10.1175/JPO-D-21-0043.1

© 2022 American Meteorological Society. For information regarding reuse of this content and general copyright information, consult the [AMS Copyright Policy](#) ([www.ametsoc.org/PUBSReuseLicenses](#)).

Ardhuin et al. 2007) and on the surface wind stress and drag coefficient (Bourassa et al. 1999; Grachev et al. 2003; Suzuki et al. 2010; Roedel et al. 2012).

Several studies have developed sea-state-dependent parameterizations of wind stress (or  $C_d$ ) in complex sea states and extreme winds (Moon et al. 2004; Hara and Belcher 2002, 2004; Fan et al. 2009; Donelan et al. 2012; Reichl et al. 2014). Because field observations in these conditions are limited, the physical mechanisms for the observed leveling off (or reduction) of  $C_d$  in extreme winds remain to be fully explained (e.g., Powell et al. 2003; Black et al. 2007; Holthuijsen et al. 2012). Donelan (2004) and Donelan et al. (2006) suggest that under strong wind forcing, airflow separation over steep waves may be an important feature that modifies  $C_d$  by causing airflow to skip over troughs and reattach at each crest, rendering the troughs invisible to the wind and reducing the overall sea surface roughness. Following from these studies, Peirson and Garcia (2008) and Grare et al. (2013) use field and laboratory results to emphasize the importance of the wave steepness  $ak$  and the pressure wave slope correlation in determining the form drag and wave growth rate. They observe a reduced wave growth rate with increasing  $ak$ , and a phase shift of the pressure field which suggests reattachment of separated airflow onto the windward face of the following wave.

Earlier studies have described airflow separation as a process which occurs only after waves have started breaking (Banner and Melville 1976; Banner 1990; Belcher and Hunt 1998; Reul et al. 2008), but recent laboratory studies using particle image velocimetry (PIV) in a wind-wave flume have captured intermittent airflow separation events over both breaking and nonbreaking waves (Veron et al. 2007; Troitskaya et al. 2011; Buckley and Veron 2016, 2019; Savelyev et al. 2020; Yousefi et al. 2020). The PIV results from a recent study by Savelyev et al. (2020) in a wind-wave tank capable of sustaining strongly energetic wave fields (e.g., high  $ak$ ) show dampened turbulent kinetic energy in the water directly below strongly forced waves possibly due to enhanced airflow separation and reduced  $C_d$ . In laboratory observations, intermittent airflow separation events have two main features in common: detachment of a high vorticity shear layer from the steep wave crest, and weak stagnant velocity in a region below (the “dead zone”). In this region, recirculation (closed streamlines) may be present in the phase-averaged flow fields shown in a reference frame moving with the wave phase speed. The recirculation patterns associated with airflow separation are distinct from those present over more mature waves for which a coherent critical layer height (where wind speed is equal to the wave phase speed) is visible above the wavy surface. It should be noted that the zero-wall stress criterion traditionally used to define separation points is not generally applicable when the fluid velocity is not zero at the boundary, e.g., flows over rotating cylinders. Boundary movement following or opposing the overlying airflow modulates separation (e.g., Gad-el Hak and Bushnell 1991).

Numerical turbulence models have been used to gain more insight into the wind turbulence over surface waves. These have included direct numerical simulations (DNS; Sullivan

et al. 2000; Yang and Shen 2010, 2017; Yang et al. 2018; Druzhinin et al. 2012; Liu et al. 2010) and large-eddy simulations (LES; Suzuki et al. 2013; Hara and Sullivan 2015; Sullivan et al. 2018a,b; Husain et al. 2019; Hao and Shen 2019; Åkervik and Vartdal 2019; Jiang et al. 2016; Yang et al. 2013; Cao and Shen 2021; Liu et al. 2010), both of which have enabled a detailed exploration of the flow characteristics that may modify the wind stress, wave growth, and dissipation over a wide range of wave parameters (e.g., wave age, wave steepness). Some have been able to reproduce laboratory observations reasonably well (Troitskaya et al. 2014; Sullivan et al. 2018b; Husain et al. 2019). In particular, Husain et al. (2019) have compared LES with the PIV results of Buckley and Veron (2016) for airflow over a train of steep, strongly forced waves in a laboratory wind-wave flume. Both model and laboratory results exhibit a phase-averaged signature of frequent airflow separation. The reasonable validation of LES results against observations by Husain et al. (2019) provides the basis for the current study to use LES to explore the airflow turbulence (occurrence and effects of intermittent airflow separation, in particular) over an extended range of wind and wave conditions expected in the open ocean.

In Part I of this study, we use the identical LES approach to explore a range of wave ages for waves following and opposing wind. A number of previous laboratory studies have addressed wind opposing waves. Young and Sobey (1985) have measured pressure fields to be nearly symmetric about the wave crest, similar to potential flow theory and consistent with previous field observations (Snyder et al. 1981; Hasselmann and Bösenberg 1991). Peirson et al. (2003) and Mitsuyasu and Yoshida (2005) have measured the evolution of waves opposing wind and have found considerable wave decay, consistent with the results of previous numerical simulations using Reynolds-averaged Navier–Stokes (RANS) equations (Al-Zanaidi and Hui 1984; Harris et al. 1995; Mastenbroek 1996; Cohen 1997). Donelan (1999) has also measured wave decay using a pressure–slope correlation, finding that the strong pressure signal in opposing wind can result in substantial form drag despite the absence of a noticeable phase shift in the dominant pressure field. A more recent modeling study of wind opposing waves by Cao et al. (2020) using wall-resolved LES finds a nearly symmetric pressure signal varying with  $ak$  and  $c/u_{*s}$ , and wave decay rates comparable to parameterizations derived from a number of the aforementioned laboratory results (see their Figs. 18 and 19). They suggest that the flow dynamics in opposing wind are mainly governed by linear processes that drive the dominant in-phase component of the flow, while nonlinear processes very close to the surface produce a small out-of-phase component that results in the modification of the form drag and wave decay rate.

Despite the existing literature, the physical mechanisms that modify the wind stress, form drag, and wave decay for waves in opposing winds are still not clearly understood. In particular, few studies have explored how waves opposing wind may enhance the effective surface roughness length and the drag coefficient, even though waves opposing wind are quite common and significantly modify the drag coefficient in

tropical cyclone conditions (Reichl et al. 2014; Chen and Curcic 2016; Chen et al. 2020). The goal of this study is to expand upon the existing literature to address how opposing wind and waves impact the turbulence in the airflow that modifies these parameters, particularly for steep waves over a range of wave phase speeds, both positive and negative, relative to wind forcing ( $c/u_{*s}$ ).

## 2. Methods

### a. Large-eddy simulation setup

We use the LES methodology identical to previous studies (Sullivan et al. 2014; Hara and Sullivan 2015; Sullivan et al. 2018b; Husain et al. 2019), which employs a pressure-driven channel flow over a wavy surface propagating through a rectangular domain with doubly periodic horizontal boundaries. This LES study entirely focuses on the airflow and the wave motion is prescribed, i.e., the wave dynamics are decoupled from those of air. We define time  $t$ , along-wave  $x$  coordinate, cross-wave  $y$  coordinate, and vertical coordinate  $z$  pointing upward with  $z = 0$  at the mean water surface. Velocities ( $u, v, w$ ) are in the ( $x, y, z$ ) directions.

Our LES uses a wave-following vertical coordinate transformed from the physical (Cartesian) coordinate such that the computational grid follows the shape of the waves close to the surface:

$$z = \zeta^{\text{LES}} + h(x, t) \left( 1 - \frac{\zeta^{\text{LES}}}{l_\zeta} \right)^3, \quad (1)$$

where  $z$  is the physical vertical coordinate,  $\zeta^{\text{LES}}$  is the computational (LES) vertical coordinate,  $h(x, t)$  is the time-varying wave shape, and  $l_\zeta$  is the vertical height of the domain (see Fig. 1 in Sullivan et al. 2014). This transformation makes the LES vertical coordinate equal to the physical vertical coordinate at the flat top boundary, where the free-slip condition is imposed (no tangential stress,  $w = 0$ ).

For most conditions in our study, we consider a linear monochromatic surface wave train with  $h(x, t) = a \cos(kx - \omega t)$ , where  $a$  is the wave amplitude,  $k$  is the wavenumber,  $\omega$  is the angular frequency, and  $c = \omega/k = \sqrt{g/k}$  is the wave phase speed. The wave orbital velocities,  $u = a\omega \cos(kx - \omega t)$  and  $w = a\omega \sin(kx - \omega t)$ , are used as the surface boundary condition for the LES. We choose a linear wave shape because we have found that the observed phase averaged wave shape of wind waves (with their wave phase determined using the Hilbert transform) is very close to the linear wave shape (Husain et al. 2019). However, for one condition, we apply the second-order nonlinear Stokes wave solution so that the bottom wave shape includes the second harmonic,  $h(x, t) = a \cos(kx - \omega t) + (1/2)ka^2 \cos(2kx - 2\omega t)$ , while the phase speed and wave orbital velocities remain identical to those of the linear deep water wave theory.

The dimensions of the computational domain are  $l_x \times l_y \times l_\zeta$ , where  $l_x = l_y = 5\lambda$  and  $l_\zeta = 2.435\lambda$ , with  $\lambda = 2\pi/k$  as the wavelength. It is discretized with  $(N_x, N_y, N_\zeta) = (256, 256, 256)$  grid points, making the horizontal resolution  $\Delta x = \Delta y =$

$0.01953\lambda$ . The vertical spacing ratio gradually increases away from the surface so that the ratio between neighboring cells is held constant at 1.0028, with the first point off the water surface located at  $\zeta_1^{\text{LES}} = 0.0065\lambda$ . In contrast to previous studies (Hara and Sullivan 2015; Sullivan et al. 2018b; Husain et al. 2019), we have expanded the vertical domain height from  $l_\zeta = \lambda$  to  $l_\zeta = 2.435\lambda$ , with double the vertical grid points (from  $N_\zeta = 128$  to  $N_\zeta = 256$ ) to allow for more prominent vertical motions away from the surface associated with higher  $c/u_{*s}$  and opposing wind conditions (see section 2d).

### b. Wind forcing

The LES setup models an environment similar to that of a wind-wave flume, where an externally imposed horizontal pressure gradient  $\partial P/\partial x$  is balanced by a surface wind stress such that  $\tau_s = (\partial P/\partial x)l_\zeta$ . Here, the stress and the pressure have been divided by air density  $\rho_a$  and have dimensions of velocity squared. The surface friction velocity is defined as  $|\tau_s| = u_{*s}^2$ . For waves following (opposing) wind at a  $0^\circ$  ( $180^\circ$ ) alignment angle, wind forcing is applied in the  $x$  direction with a negative (positive) external pressure gradient  $\partial P/\partial x$  that yields a negative (positive) surface stress  $\tau_s$ . Because the pressure gradient is constant with height, the total wind stress magnitude decreases linearly to zero at the ceiling where the free-slip condition is imposed. Recent studies have compared LES model results to laboratory measurements of turbulent airflow in a wind-wave flume under strongly forced conditions (e.g., Sullivan et al. 2018b; Husain et al. 2019), finding that LES can accurately reproduce the mean wind profile, momentum flux budget, and phase-averaged turbulent flow fields using an idealized wind-wave channel setup. Furthermore, these results show that the turbulence fields in the wave boundary layer (where they are modified by surface waves) are not significantly affected by the linearly decreasing wind stress in contrast to those in the constant stress layer in open ocean conditions.

### c. Subgrid-scale and surface roughness parameterizations

Turbulent flow in LES is spatially filtered such that dominant-scale turbulence is resolved while subgrid-scale (SGS) fluxes below a filter threshold are parameterized using a conventional TKE-closure SGS parameterization described in more detail in Moeng (1984), Sullivan et al. (2014), and Moeng and Sullivan (2015), and used by Hara and Sullivan (2015), Sullivan et al. (2018b), Husain et al. (2019), and a number of other studies.

Similar to previous studies, we employ a wall-modeled LES. Along the wavy surface, the local instantaneous tangential stress is parameterized based on the local instantaneous mean wind shear (determined from the difference between the surface tangential water velocity and the tangential wind velocity at the first grid point off the surface) by applying the law of the wall (a log profile) with a prescribed background surface roughness length  $z_{ob}$ . The parameter  $z_{ob}$  represents the bulk effect of viscosity (which is more important in laboratory conditions) and subgrid roughness elements such as

higher frequency waves (which dominate in open ocean conditions) on the local frictional stress.

In previous studies (Hara and Sullivan 2015; Sullivan et al. 2018b), the normalized background surface roughness has been set at  $kz_{ob} = 2.7 \times 10^{-3}$  to represent typical strongly forced wind-wave conditions in a laboratory setting. In open ocean conditions with a spectrum of waves,  $kz_{ob}$  likely varies significantly depending on wind speed, the scale of resolved waves of interest, and other environmental factors such as surfactants. It is also expected that  $z_{ob}$ , which represents unresolved wave effects, should vary with the phase of the resolved waves because shorter waves are known to be modulated by longer waves (e.g., Gent and Taylor 1976; Gent 1977; Kudryavtsev and Makin 2002).

In our recent study (Husain et al. 2019) we have systematically investigated how varying  $kz_{ob}$  affects the airflow turbulence over steep waves ( $ak = 0.27$ ) in strongly forced conditions. The results show that the flow field is quite sensitive to the  $z_{ob}$  value specified near the crest; a higher  $z_{ob}$  increases the frequency of intermittent airflow separation events and enhances the resulting signature in the phase averaged flow fields. However, the airflow is hardly affected if the  $z_{ob}$  value is altered away from the crest. In the same study, the effect of wave-phase-dependent surface drift velocity has been investigated as well. The results indicate that the drift velocity added near the wave crest simply increases the wind speed by the same amount everywhere without affecting the airflow turbulence characteristics, and that the drift velocity added away from the crest has very little impact.

Since the effects of varying  $z_{ob}$  and surface drift have been investigated previously, in this study we keep the normalized background surface roughness held constant at  $kz_{ob} = 2.7 \times 10^{-3}$  and impose zero surface drift velocity for all simulations; that is, we do not repeat the sensitivity study of varying roughness length and drift velocity, acknowledging that their impacts are potentially important. We then focus on investigating the effects of varying wind forcing  $c/u_{*s}$  on the wind turbulence, wave form drag, effective surface roughness length (which includes the effect of resolved waves), and drag coefficient.

Note that since our logarithmic wall model is based on the assumption of turbulence in equilibrium, its applicability may be questionable where flow separation occurs. However, our previous study (Husain et al. 2019) shows that changing the roughness value below flow separation areas (away from the wave crest) in strongly forced cases has little impact on the results, suggesting that our LES results are not very sensitive to the wall modeling in such areas.

#### d. Simulations

While the actual LES of waves opposing wind is performed by reversing the wind direction as described above, in the following sections we differentiate waves following wind and waves opposing wind by the sign of the wave phase speed  $c$ ; that is, the wind always blows in the positive  $x$  direction (wind stress  $\tau_x$  is always negative), and the waves propagate in the positive/negative  $x$  direction for following/opposing cases.

TABLE 1. List of run conditions and results of roughness enhancement  $z_o/z_{ob}$  and nondimensional wave growth/decay coefficient  $c_\beta$  for 11 LES simulations. The letters “f” and “o” in the run name represent waves following and opposing wind, respectively. The letter “s” in the run name represents Stokes waves. Nondimensional parameters used in LES cases include wave age ( $c/u_{*s}$ , which is negative for wind opposing wind), wave steepness ( $ak$ ), and parameterized background roughness length ( $kz_{ob}$ ). Wave steepness is held constant for all simulations at  $ak = 0.2665$  ( $ak \sim 0.27$ ). Parameterized background roughness is also held constant at  $kz_{ob} = 2.70 \times 10^{-3}$ . The values for  $c_{\beta t}$ ,  $c_{\beta n}$ , and  $c_{\beta p}$  refer to tangential turbulent stress, normal turbulent stress, and pressure contributions to  $c_\beta$ , and  $c_{\beta tot}$  is the total.

Run	$c/u_{*s}$	$z_o/z_{ob}$	$c_{\beta t}$	$c_{\beta n}$	$c_{\beta p}$	$c_{\beta tot}$
1.4f	1.4	4.7	2.8	1.6	13.6	18.0
1.4fs	1.4	5.8	2.2	1.3	14.8	18.2
1.4o	-1.4	7.0	-3.5	-0.5	-13.1	-17.2
2.8f	2.8	4.0	2.0	1.8	13.9	17.7
2.8o	-2.8	8.7	-3.9	0.0	-13.2	-17.1
5.6f	5.6	4.1	0.1	1.3	13.8	15.2
5.6o	-5.6	14.9	-4.8	1.1	-14.6	-18.3
8.2f	8.2	3.0	-1.3	0.6	10.9	10.3
8.2o	-8.2	20	-5.8	1.8	-16.9	-20.9
11.0f	11.0	1.58	-2.5	-0.1	6.6	3.9
11.0o	-11.0	32	-7.1	2.1	-19.8	-24.9

In total, we perform simulations for five wave ages in following wind ( $c/u_{*s} = 1.4, 2.8, 5.6, 8.2, 11$ ) and five cases in opposing wind ( $c/u_{*s} = -1.4, -2.8, -5.6, -8.2, -11$ ) with a wave slope held constant at  $ak = 0.27$ . For wind following waves at  $c/u_{*s} = 1.4$ , we include results for a Stokes wave as described in section 2a. This range of wave ages and the wave slope are similar to that of Sullivan et al. (2018a) for waves following wind. We choose to focus on a wave slope at the steeper end of those observed in the field because we are particularly interested in the impacts of intermittent airflow separations (or separation-like flows, as described later) that are more common with steep waves (Donelan et al. 2006, see their Fig. 6), and because this study is motivated by its potential application in tropical cyclone conditions where waves opposing wind are common and often steep.

Each simulation is run for approximately 130 000 time steps and averaged over the last 60 000 time steps after the wind field has reached a statistically steady state. Sullivan et al. (2014) and Sullivan et al. (2018b) provide a full description of the LES algorithm and numerical methods used to solve the governing equations. See Table 1 for more details on the conditions simulated in this study.

#### e. Data analysis

For our data analysis, we first map the LES coordinate  $\zeta^{\text{LES}}$  back to the  $z$  coordinate, and then introduce a horizontal coordinate  $\xi$  that moves with the wave phase speed

$$\xi = x - ct. \quad (2)$$

Some initial analyses are made in the rectangular ( $\xi, z$ ) coordinate in which the waves are no longer time varying.

However, most results are analyzed after the  $z$  axis is remapped to a vertical wave following coordinate  $\zeta$  that exponentially approaches toward the  $z$  coordinate (Hara and Sullivan 2015):

$$z = \zeta + a \cos(k\xi)e^{-k\zeta} \quad (3)$$

for a linear wave or

$$z = \zeta + a \cos(k\xi)e^{-k\zeta} + ka^2 \cos(2k\xi)e^{-2k\zeta} \quad (4)$$

for the Stokes wave, with the Jacobian of coordinate transformation,

$$J = \frac{\partial \zeta}{\partial z}. \quad (5)$$

We use the mapping (3) or (4)—instead of the LES mapping (1)—for data analysis since this mapping is more common in previous studies and is not affected by the vertical extent of the LES domain size, which is different between Part I and Part II (Husain et al. 2021). In this coordinate system, we employ a triple decomposition to separate all quantities into mean, turbulent, and wave-coherent components, similar to previous studies (e.g., Sullivan et al. 2000; Chalikov and Rainchik 2011; Hara and Sullivan 2015; Buckley and Veron 2016) using

$$\psi = \bar{\psi} + \psi' = \langle \psi \rangle + \tilde{\psi} + \psi', \quad (6)$$

where  $\bar{\psi}$  is the wave phase average (average in  $t$  and  $y$ ),  $\langle \psi \rangle$  is the horizontal mean (average in  $\xi$ ),  $\tilde{\psi}$  is the wave-coherent fluctuation component, and  $\psi'$  is the turbulent fluctuation component. This approach allows us to define wave-coherent and turbulent fluxes as separate components of the total wind stress. Specifically, the horizontally averaged  $x$ -momentum equation may be expressed as

$$\frac{\langle \tau^w \rangle + \langle \tau^p \rangle}{\tau_s} + \frac{\langle \tau^t \rangle}{\tau_s} + \frac{\partial P}{\partial x} \frac{\zeta}{\tau_s} = 1, \quad (7)$$

where  $\langle \tau^w \rangle = \langle \bar{u} \bar{W} \rangle$  is the wave-coherent stress and  $\langle \tau^t \rangle = \langle u' W' \rangle$  is the turbulent stress that includes both resolved and parameterized subgrid-scale stresses. Notice that these stresses are defined using a contravariant vertical velocity perpendicular to a constant  $\zeta$  surface

$$W = \frac{1}{J} u \frac{\partial \zeta}{\partial x} + w, \quad (8)$$

such that  $uW$  represents flux of  $x$  momentum across the constant  $\zeta$  surface due to the advective velocity  $W$  (Hara and Sullivan 2015). The pressure (form) stress,

$$\langle \tau^p \rangle = \left\langle \frac{1}{J} \bar{p} \frac{\partial \zeta}{\partial x} \right\rangle, \quad (9)$$

represents momentum flux due to pressure applied on a tilted constant  $\zeta$  surface. The sum of the three stress components is equal to the total wind stress  $\langle \tau^{\text{tot}} \rangle = \langle \tau^w \rangle + \langle \tau^p \rangle + \langle \tau^t \rangle$ , whose magnitude linearly decreases from the surface. At the

wavy surface ( $\zeta = 0$ ) the wave coherent stress  $\langle \tau^w \rangle$  is zero and the total wind stress  $\tau_s$  is a sum of the pressure form drag  $\langle \tau^p \rangle$  and the (subgrid) turbulent stress  $\langle \tau^t \rangle$ ; the latter represents the momentum flux into unresolved waves and the surface viscous stress contribution. For more details on the triple decomposition and the derivation of the continuity, momentum, and energy equations in this mapped coordinate, refer to Hara and Sullivan (2015).

### 3. Results and discussion

#### a. Two-dimensional phase averaged airflow above waves following wind

In this section all flow fields presented are normalized by  $u_{*s}$  and  $k$ . Figures 1–3 display the two-dimensional phase-averaged flow fields for the cases of  $c/u_{*s} = 11, 5.6,$  and  $1.4$  (waves following wind, top panels) and  $c/u_{*s} = -1.4, -5.6,$  and  $-11$  (waves opposing wind, bottom panels). Figure 1 shows the streamlines, streamwise velocity  $[(\bar{u} - c)/u_{*s}]$ , and vertical velocity  $(\bar{w}/u_{*s})$ . Figure 2 shows pressure  $(\bar{p}/u_{*s}^2)$ . In the rightmost column of Fig. 2, the surface profiles are shown for the total normal stress (pressure plus the turbulent normal stress), pressure only, and the turbulent tangential stress. Figure 3 includes the TKE  $[\bar{e}/u_{*s}^2 = (\overline{u'u'} + \overline{v'v'} + \overline{w'w'})/(2u_{*s}^2)]$ , dissipation rate  $[\epsilon/(ku_{*s}^3)]$ , and the spanwise vorticity  $\{\bar{\omega}_y/(ku_{*s}) = [(\partial \bar{u}/\partial z) - (\partial \bar{w}/\partial x)]/(ku_{*s})\}$ . Note that the dissipation rate  $\epsilon$  is solved in the SGS turbulent kinetic energy equation [see Eqs. (1d) and (11) in Sullivan et al. 2014]. All the quantities are plotted in the rectangular  $(\xi - z)$  coordinate that moves with the wave, so that the phase averaged flow field is independent of  $t$ . In addition, the results are plotted in the mapped  $(\xi - \zeta)$  coordinate with the vertical axis in a log scale so that the flow fields very close to the wavy surface can be clearly observed. Wind is blowing from left to right, and waves are propagating from left to right (right to left) in the following (opposing) cases (before the coordinate transformation). Note that the streamline field has been constructed from  $\bar{u} - c$  and  $\bar{w}$ .

First, we examine the cases of waves following wind (top three panels of Figs. 1–3). In the case of strongly forced waves at  $c/u_{*s} = 1.4$  (third row from top), contours of constant  $\bar{u} - c$  expand away from the surface downstream of the crest with reduced velocity and a small recirculation bubble on the leeward side of the crest (Figs. 1c,i). Inside this bubble, the TKE, dissipation rate, and vorticity are all significantly reduced (Figs. 3c,i,o, and more clearly seen in Figs. 3C,I,O in the mapped coordinate with the vertical log scale). The high vorticity layer at the wave crest is detached from the surface and extends downstream of the crest above the recirculation bubble (Figs. 3o,O), indicating large streamwise velocity just above this high vorticity layer. The elevated TKE above the crest appears to be advected by the detached high velocity and intensifies, extending just above the high vorticity layer (Figs. 3c,C). These patterns are identical to the LES results presented in Husain et al. (2019) for the same wave age ( $c/u_{*s} = 1.4$ ) and wave slope ( $ak = 0.27$ ).

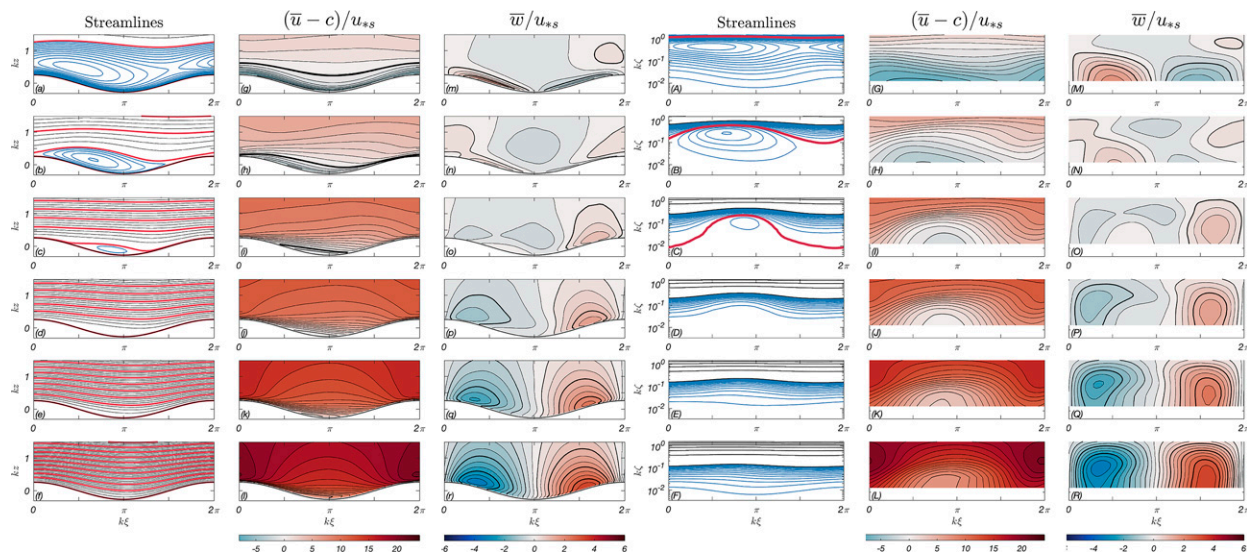


FIG. 1. (left three columns) Normalized phase-averaged flow fields in the  $\xi$ - $z$  coordinate and (right three columns) the mapped  $\tilde{\xi}$ - $z$  coordinate for (top three rows) waves following wind ( $c/u_{*s} = 11.0, 5.6, 1.4$ ) and (bottom three rows) waves opposing wind ( $c/u_{*s} = -1.4, -5.6, -11.0$ ) from left to right: streamlines, horizontal velocity  $[(\bar{u} - c)/u_{*s}]$ , and vertical velocity  $(\bar{w}/u_{*s})$ . To capture the range of wind speeds (including recirculating wind close to the surface), the spacing between streamlines is decreased by a factor of 4 from red to black, and by a factor of 7 from black to blue.

Buckley and Veron (2016) have been able to demonstrate with high-resolution particle image velocimetry (PIV) that near-surface wind flow patterns are modified by transient, sporadic detachment of airflow from the crests of steep, young waves. Instantaneous measurements of  $u$  and  $w$  over laboratory waves capture a layer of enhanced spanwise vorticity developing and ejecting away from the wave crest, resulting in weak, stagnant, sometimes negative airflow in the trough (see Buckley and Veron 2016, their Fig. 6). Previous LES results (e.g., Hara and Sullivan 2015; Sullivan et al. 2018b), and a more recent comparison between these observations and LES by Husain et al. (2019), have also found that intermittent airflow separation events can occur frequently over steep, nonbreaking waves, and their phase-averaged character in observations can be well reproduced in LES. This suggests that while these separation events are not persistent in either the observations or LES, they occur frequently enough in steep, strongly forced conditions to leave a signature in the phase-averaged flow fields.

These intermittent airflow separation events also affect the phase-averaged pressure field (Figs. 2c,C,G). It is well known that the pressure-wave slope correlation determines the form drag and the wave growth rate (e.g., Peirson and Garcia 2008; Grare et al. 2013), but the role of airflow dynamics in shifting the phase and magnitude of maximum surface pressure is still not well understood. The LES results of Sullivan et al. (2018b) associate the location and magnitude of maximum pressure with reattachment of detached flow onto the windward face of the following wave. Our results also suggest that the reattachment of the separated flow influences the location of the high pressure on the windward face of the wave (Figs.

2c,C,G) and the resulting form drag and wave growth rate (discussed in section 3g).

As the wave age ( $c/u_{*s}$ ) increases for waves following wind, the recirculation bubble (or “cat’s eye” pattern) grows larger (see expanding blue streamlines in Figs. 1b,a), indicating that the critical layer expands away from the surface with increasing wave age (note that the wind speed is equal to the wave phase speed at the top of the critical layer). At the same time, the signature of intermittent airflow separation (reduced TKE,  $\epsilon$ , and  $\bar{\omega}_y$  inside the recirculation bubble; layers of enhanced TKE,  $\epsilon$ , and  $\bar{\omega}_y$  separated from the wave crest and extended above the bubble) rapidly diminish at higher wave ages (Figs. 3B,A,H,G,N,M). The enhanced  $\epsilon$  and  $\bar{\omega}_y$  remain attached to the surface and appear to shift upstream from the crest to the trough region (Figs. 3H,G,N,M). Consistent with the trends shown in Sullivan et al. (2018a), the near-surface vertical velocity  $\bar{w}$  becomes more negatively correlated with the local wave slope as the wave age increases (Figs. 1n,m,N,M). Sullivan et al. (2018a) speculate that these shifting patterns could be due in part to critical layer dynamics that generate waves via shear flow at the height where wind speed is equal to the wave phase speed. They also suggest that faster waves produce an effect more closely associated with a wave driving (or “boundary pumping”) regime, whereby the undulation of the wavy surface drives near-surface  $\bar{w}$  via the wave’s surface tilt interacting with the wave phase speed. Cao and Shen (2021) also point out that the vertical velocity  $\bar{w}$  is associated with the airflow perturbation induced by the vertical wave movement in their simulation with a similar wave age.

Unlike the slow wave case ( $c/u_{*s} = 1.4$ ), the region of low pressure for the intermediate case ( $c/u_{*s} = 5.6$ ) occurs along the leeward face of the wave rather than at the top of the crest

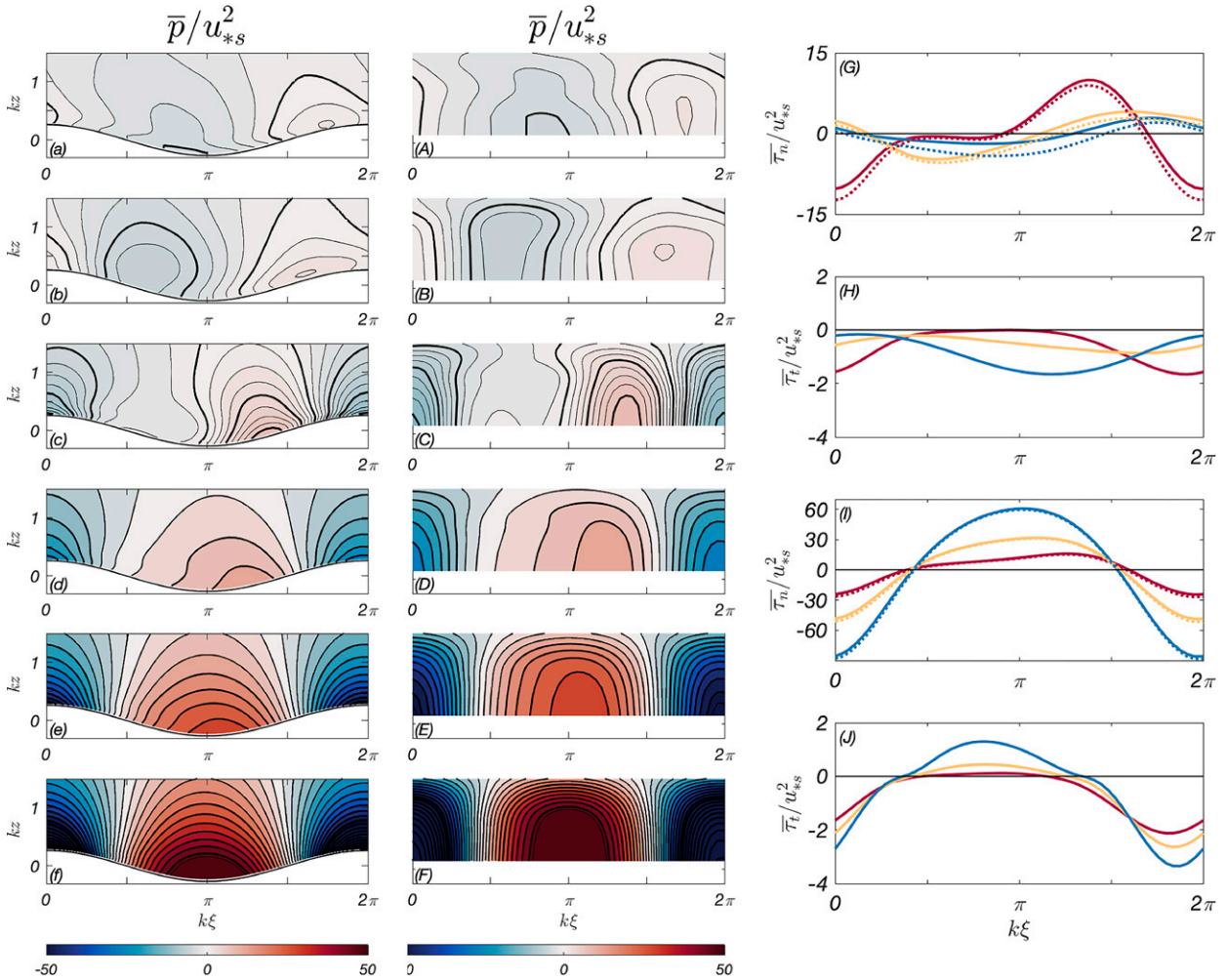


FIG. 2. (left) Normalized phase-averaged flow fields in the  $\xi$ - $z$  coordinate and (center) the mapped  $\xi$ - $\zeta$  coordinate for (top three rows) waves following wind ( $c/u_{*s} = 11.0, 5.6, 1.4$ ) and (bottom three rows) waves opposing wind ( $c/u_{*s} = -1.4, -5.6, -11.0$ ) of pressure ( $\bar{p}/u_{*s}^2$ ). (right) The surface stress distribution for the normal stress  $\bar{\tau}_n/u_{*s}^2$  (panels labeled G and I; solid line is total normal stress and dotted line is pressure only) and for the tangential stress  $\bar{\tau}_t/u_{*s}^2$  (panels labeled H and J) for  $|c/u_{*s}| = 1.4, 5.6,$  and  $11.0$  (dark red, light orange, blue). The bottom two panels are for waves opposing wind.

(Figs. 2b,B,G), potentially associated with a nonseparated “sheltering effect” (e.g., Belcher and Hunt 1993, 1998). The low pressure region further moves toward the trough for faster waves ( $c/u_{*s} = 11$ , Figs. 2a,A,G). The magnitude of the pressure variation diminishes (Fig. 2G), and so too do the wave growth rate and form drag as the wave age increases (discussed in section 3g).

*b. Two-dimensional phase averaged airflow above waves opposing wind*

Next, we examine the cases of waves opposing wind (bottom panels in Figs. 1-3). One immediately notices that the flow field is dominated by a strong pressure perturbation (Figs. 2d-f,D-F) in phase with  $-h$  (negative of the wave elevation), and a strong vertical velocity perturbation (Figs.

1p-r,P-R) in phase with  $\partial h/\partial x$  (the wave slope). This result is consistent with the wall-resolved LES results of Cao et al. (2020) for waves opposing wind, as well as previous laboratory and field measurements (Snyder et al. 1981; Young and Sobey 1985; Hasselmann and Bösenberg 1991). Cao et al. (2020) show that these flow features are well explained by a simple linear inviscid model. This trend of increasingly stronger along-wave pressure gradient is reminiscent of potential flow, as observed by Young and Sobey (1985). However, the pressure field in phase of  $-h$  does not contribute to the wave growth rate or the form drag; only the small out-of-phase component does. Cao et al. (2020) discuss how the strong turbulence very near the surface plays an important role in determining the magnitude of this component.

Similarly, our results show that the near surface turbulence fields contain strong wave induced perturbations. The most

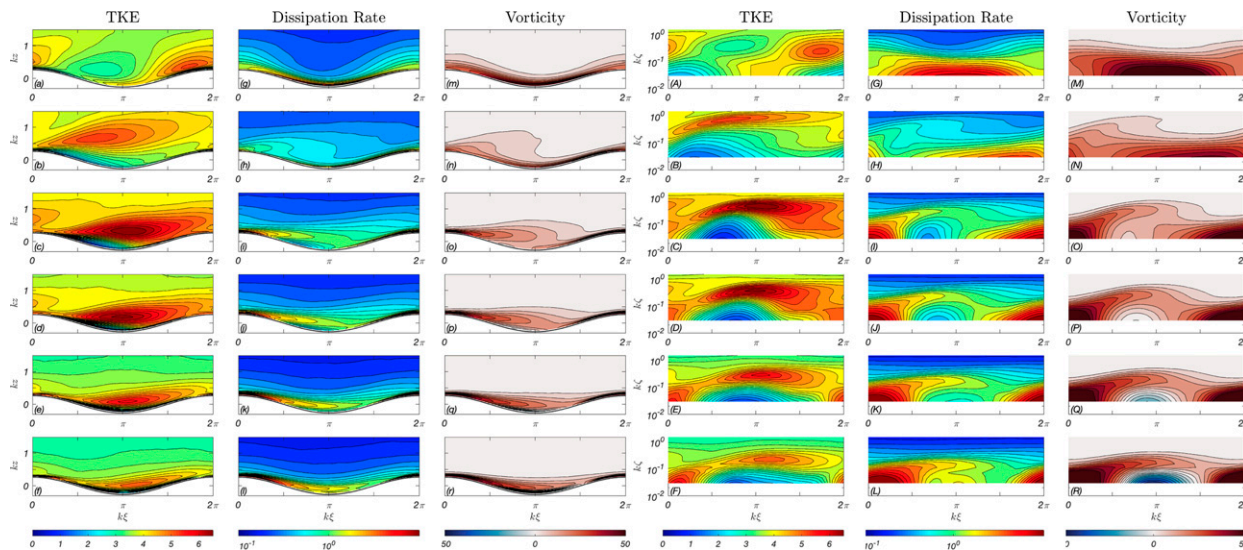


FIG. 3. (left three columns) Normalized phase-averaged flow fields in the  $\xi$ - $z$  coordinate and (right three columns) the mapped  $\xi$ - $\zeta$  coordinate for (top three rows) waves following wind ( $c/u_{*s} = 11.0, 5.6, 1.4$ ) and (bottom three rows) waves opposing wind ( $c/u_{*s} = -1.4, -5.6, -11.0$ ) from left to right: turbulent kinetic energy ( $\bar{e}/u_{*s}^2$ ), dissipation rate [ $\epsilon/(ku_{*s}^3)$ ], and spanwise vorticity [ $\bar{\omega}_y/(ku_{*s})$ ].

notable feature near the wavy surface is that there is a clear progression in the flow structure from positive to negative wave ages (more specifically, from large positive to small positive to small negative to large negative wave ages; that is, from top to bottom in Figs. 1–3). In particular, the flow fields of TKE,  $\epsilon$ , and  $\omega_y$  are surprisingly similar between the cases of  $c/u_{*s} = 1.4$  (waves following wind, Figs. 3C,I,O) and  $c/u_{*s} = -1.4$  (waves opposing wind, Figs. 3D,J,P). In both cases, the common signatures are observed (reduced TKE,  $\epsilon$  and  $\omega_y$  in the dead zone downstream of the crest; layers of enhanced TKE,  $\epsilon$ , and  $\bar{\omega}_y$  detached from the crest above). In the case of waves following wind, these features are associated with intermittent airflow separations. Even though the cases with waves opposing wind exhibit these same features in Fig. 3, they nevertheless do not exhibit separation because the wind speed along the wave surface is positive (even near the trough) in a reference frame moving with the wave. Nevertheless, our results at  $c/u_{*s} = -1.4$  suggest that a strong wind shear develops above the wave crest and generates large TKE and a detached high vorticity (high wind shear) layer from the crest, which extends over a region of reduced vorticity above the leeward trough. The elevated TKE above the crest is advected by the enhanced streamwise velocity, and shows intensification just above the detached high vorticity layer downstream of the crest.

As the wave speed increases from  $c/u_{*s} = 1.4$  to  $-5.6$  and  $-11$ , these flow characteristics remain similar but slowly evolve. The elevation of the detached enhanced layers of TKE,  $\epsilon$ , and  $\bar{\omega}_y$  gradually decreases, and the location of the region of reduced TKE,  $\epsilon$ , and  $\bar{\omega}_y$  extends toward the trough (Figs. 3E,F,K,L,Q,R). This evolution is likely due to the increasing streamwise background flow in the reference frame moving with the wave. Nevertheless, all the flow characteristics associated with the detached high vorticity layer persist.

One surprising feature is that  $\bar{\omega}_y$  is not only reduced, but becomes significantly negative below the detached high vorticity layer as  $c/u_{*s}$  becomes more negative (Figs. 3Q,R). The velocity fields in Figs. 1K,L,Q,R suggest that this negative vorticity is due to a combination of decreasing  $\partial\bar{u}/\partial z$  and increasing  $\partial\bar{w}/\partial x$ . In particular, Fig. 1L shows that the wind shear  $\partial\bar{u}/\partial z$  becomes negative in a small region just above the trough—that is, wind speed is decreasing with height (notice that the velocity contours tilt more than  $90^\circ$  there). In the case of waves following wind, such negative wind shear is usually associated with strongly separating flows above actively breaking waves, but it does not occur in the phase-averaged flow fields over nonbreaking waves in our LES simulations. For the case of waves opposing wind, negative wind shear near the trough appears to be more common and persistent, suggesting that the flow perturbations just downstream of the wave crest become stronger as  $c/u_{*s}$  becomes more negative, even if they are not associated with apparent airflow separations and their vertical extent is somewhat reduced. Note that the persistence of airflow separations is often associated with a small region of recirculation (closed streamlines distinct from those present over more mature waves, as in Fig. 1a,b) for young waves following wind in a reference frame moving with the wave phase speed (see the streamlines for  $c/u_{*s} = 1.4$ , Fig. 1c), but this pattern is absent for all waves opposing wind in a reference frame moving with the opposing wave phase speed. Although these streamline patterns are absent for opposing waves, the flow perturbation (enhanced negative  $\bar{\omega}_y$ , reduced TKE, reduced  $\epsilon$ ) intensifies regardless.

Although the pressure field appears dominated by the perturbation in phase with  $-h$ , a significant out-of-phase component exists which is not apparent in the flow fields, but

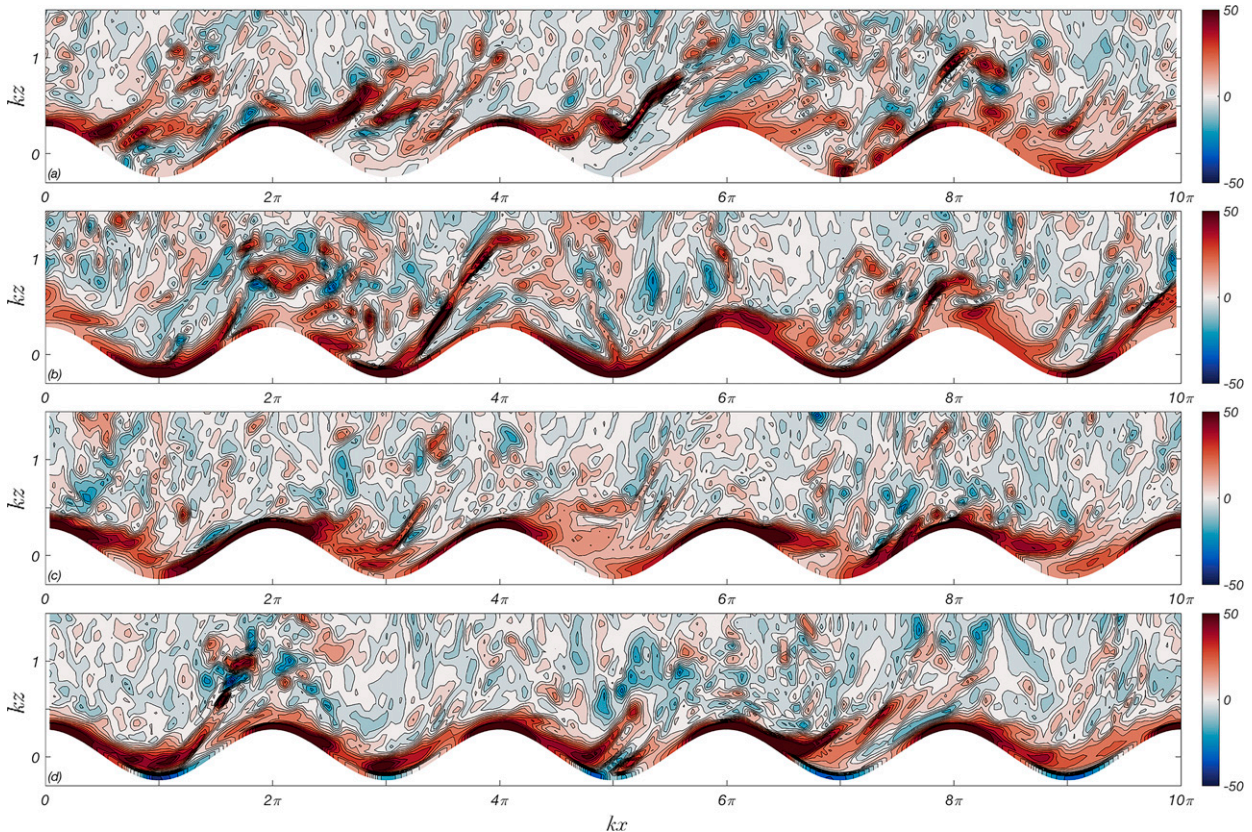


FIG. 4. Normalized instantaneous vorticity fields  $[\omega_y/(ku_{*s})]$  in the  $x$ - $z$  coordinate for (top two rows) waves following wind ( $c/u_{*s} = 1.4, 11.0$ ) and (bottom two rows) waves opposing wind ( $c/u_{*s} = -1.4, -11.0$ ).

nonetheless results in an increase of the form drag and wave decay rate as  $c/u_{*s}$  decreases (Figs. 2d-f,D-F,I)—see section 3g for more discussion. It is feasible that the increasingly intensified perturbation downstream of the crest that is apparent in the flow fields of TKE, dissipation rate and vorticity may be (at least partially) responsible for this development.

*c. Instantaneous airflow features*

To demonstrate the transient character of the flow field over a range of  $c/u_{*s}$ , we display instantaneous snapshots of spanwise vorticity  $\omega_y$  for  $c/u_{*s} = 1.4, 11, -1.4,$  and  $-11$  in Fig. 4. Slower waves following wind ( $c/u_{*s} = 1.4$ , Fig. 4a) generate enhanced positive vorticity along the windward face of the wave crest. This layer of enhanced vorticity intermittently separates from the leeward face of the crest, coupled with reduced (sometimes negative) vorticity below. The detachment location, trajectory, and magnitude of the enhanced vorticity layer significantly vary from wave to wave.

With faster waves at  $c/u_{*s} = 11$  (Fig. 4b) detachment of enhanced positive vorticity from the crest is not apparent. Instead, the vorticity field is dominated by a thin high vorticity layer along the entire wave surface and signatures of ejections and sweeps (motion of air away from and toward the surface), which are characteristic of near-wall turbulent boundary layers over flat walls. The locations of ejections and sweeps

appear uncorrelated with the wave phase. These features are consistent with the instantaneous flow fields captured by Buckley and Veron (2019) using high-resolution PIV in a wind-wave flume over a similar range of wave ages.

In the case of slow waves opposing wind ( $c/u_{*s} = -1.4$ , Fig. 4c), the instantaneous flow patterns are quite similar to those of slow waves following wind ( $c/u_{*s} = 1.4$ , Fig. 4a), except that the height of the intermittent detached high vorticity layer appears to be suppressed. As the wave speed increases ( $c/u_{*s} = -11$ , Fig. 4d), the height of the detached high vorticity layer is further reduced but persistent negative vorticity regions appear near the trough, consistent with the phase-averaged vorticity field (Fig. 3R).

*d. Vertical profiles of horizontally averaged wind fields*

In the following subsections we investigate the vertical profiles (dependence on  $\zeta$ ) of wind variables averaged horizontally in the mapped coordinate (mean wind speed, mean wind shear, mean TKE, and the terms in the momentum and energy budget equations) as well as the enhancement of the equivalent surface roughness due to waves and the wave growth (decay) rates for waves following (opposing) wind. In particular, we attempt to explain how these quantities are affected by the physical mechanisms identified in the two-dimensional flow analysis in the previous subsections. All the

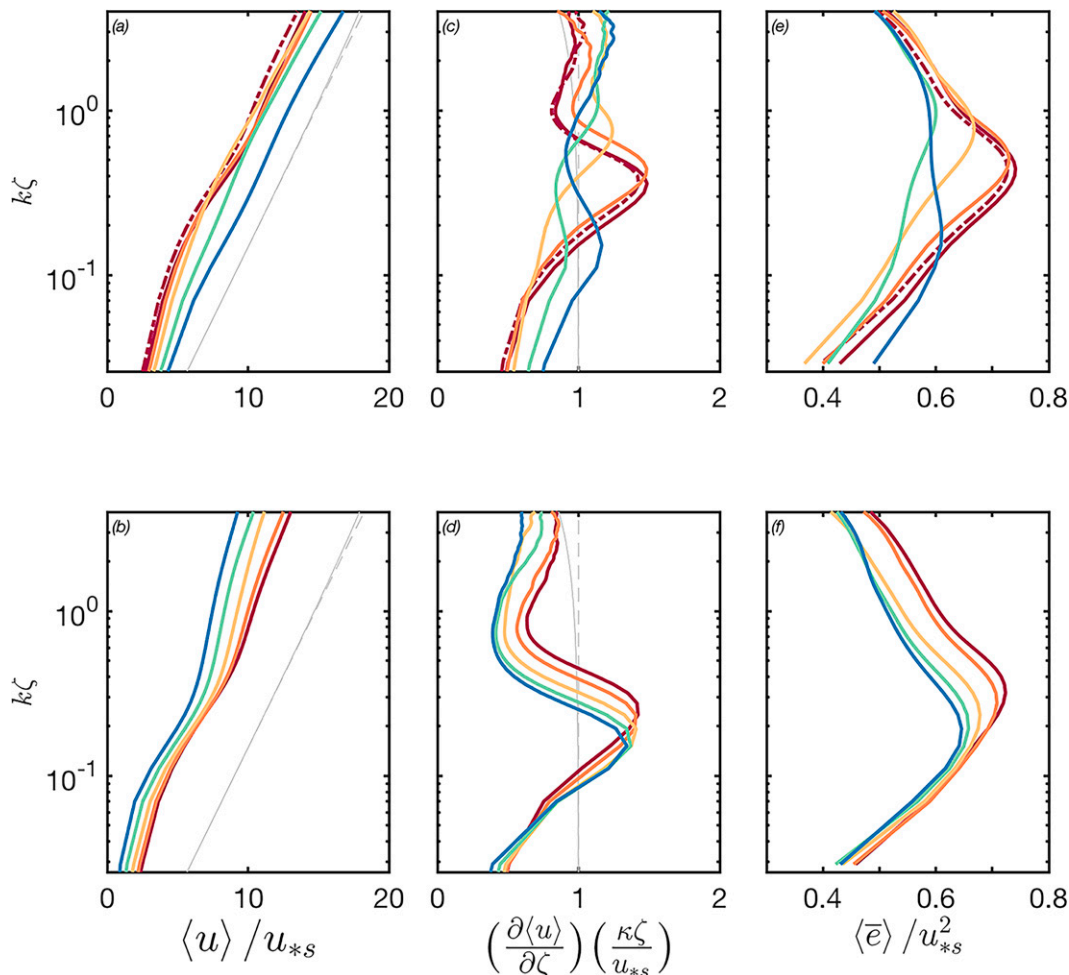


FIG. 5. Normalized vertical profiles of horizontally averaged wind speed ( $\langle u \rangle / u_{*s}^2$ ), wind shear  $[(\partial \langle u \rangle / \partial \zeta)(\kappa \zeta / u_{*s})]$ , and TKE ( $\langle \bar{e} \rangle / u_{*s}^2$ ) for (top) waves following wind and (bottom) waves opposing wind for  $|c/u_{*s}| = 1.4, 2.8, 5.6, 8.2,$  and  $11.0$  (dark red, dark orange, light orange, light green, and blue). The dot-dashed dark red line is the Stokes wave case for  $c/u_{*s} = 1.4$ . Gray lines are profiles over a flat wall as explained in the main text.

profiles are displayed up to  $k\zeta = 4$  because the results above this elevation are affected by the reduced wind stress and the LES top boundary.

Figures 5a–f display normalized horizontal mean profiles of wind speed ( $\langle u \rangle / u_{*s}$ ), wind shear  $[(\partial \langle u \rangle / \partial \zeta)(\kappa \zeta / u_{*s})]$ , and TKE ( $\langle \bar{e} \rangle / u_{*s}^2$ ). The upper panels show results with waves following wind at  $c/u_{*s} = 1.4, 2.8, 5.6, 8.2,$  and  $11$  (with increasing  $c/u_{*s}$  transitioning from warmer to cooler colors), and the lower panels show results with waves opposing wind at  $c/u_{*s} = -1.4, -2.8, -5.6, -8.2,$  and  $-11$  (with increasingly negative  $c/u_{*s}$  transitioning from warmer to cooler colors). The red dot-dashed line in the upper panels represents  $c/u_{*s} = 1.4$  with a first-order nonlinear Stokes wave including the second harmonic applied to the bottom wave shape.

For waves following wind (Fig. 5a), the far field wind profiles above the wave boundary layer (above about  $k\zeta = 1$ ) are roughly parallel to, but shifted to the left of, the wind profile over a flat surface with a nondimensional background surface

roughness of  $kz_{ob} = 2.7 \times 10^{-3}$  (gray lines). Here, the solid gray line represents the wind profile modified by the linearly decreasing wind stress in  $k\zeta$ , and the dashed gray line is the wind profile for constant stress in  $k\zeta$ . Since the background roughness length (accounting for the form drag of unresolved small waves and the viscous stress) along the wavy surface is identically set at  $kz_{ob} = 2.7 \times 10^{-3}$  in all simulations, the decrease of the far field wind speed indicates that the waves enhance the effective roughness length  $z_o$  (determined by extrapolating the wind profile above the wave boundary layer toward the surface) relative to the background roughness length  $z_{ob}$ .

Specifically, for each case we roughly estimate  $z_o$  by horizontally shifting the flat wall wind profile (gray solid line) to match the wind speed above the wave boundary layer (matching the wind speed at  $k\zeta = 4$  for simplicity), then we find the height where the shifted flat wall wind speed becomes zero. We find that the slowest waves ( $c/u_{*s} = 1.4$ ) produce the

largest  $z_o$  ( $z_o/z_{ob} = 4.65$ ), which rapidly decreases to  $z_o/z_{ob} = 1.58$  as  $c/u_{*s}$  increases to 11 (see Table 1 for a summary). This trend is consistent with the findings from a DNS study of idealized water waves in Couette flow over a similar range of  $c/u_{*s}$  with  $ak = 0.1, 0.2$  (Sullivan et al. 2000) and the results of Sullivan et al. (2018a) for similar  $c/u_{*s}$  and  $ak$ . Note that the case using the second-order Stokes wave for  $c/u_{*s} = 1.4$  (Run 1.4fs) produces a 25% higher  $z_o$  compared to its sinusoidal counterpart (Run 1.4f). The 25% increase in  $z_o$  is not necessarily a large impact on wind stress or the drag coefficient. For example, for 10-m wind speed of  $10 \text{ m s}^{-1}$  and  $z_o$  of 0.14 mm, the 25% increase of  $z_o$  corresponds to wind stress (drag coefficient) increase by 4%. Nevertheless, such wave nonlinearity effects are certainly significant, and our results in other cases likely contain minimum 25% uncertainty attributable to wave nonlinearity.

The mean normalized wind shear is shown in Fig. 5c. Similar to the gray lines for mean wind speed in Fig. 5a, gray lines here represent the mean wind shear profile unmodified by waves for linearly decreasing wind stress in  $k\zeta$  (solid) and constant wind stress in  $k\zeta$  (dashed). When the wind shear profile deviates to the right (left) of the gray solid line, the wind shear is enhanced (reduced) due to the wave effect. Since the mean wind speed must approach zero at the background roughness height in all simulations ( $z = z_{ob}$ ), the shift of the far field wind profile relative to the flat wall profile means that the mean wind shear is modified by waves inside the wave boundary layer. Here, the normalized mean wind shear is defined and plotted such that the area integral of its deviation from the flat wall case is approximately proportional to the deviation of the normalized far field mean wind speed from the flat wall profile (see Fig. 2 and discussion in Hara and Sullivan 2015).

For waves following wind, the wave age plays a significant role in the character of the mean wind shear. Slower waves ( $c/u_{*s} = 1.4, 2.8$ ) show enhanced wind shear slightly above the height of the wave crest and reduced wind shear toward the surface. This pattern has been observed for similar wave ages in the LES results of Husain et al. (2019), where we describe the enhanced mean wind shear as a signature of frequent airflow separations due to the averaged effect of enhanced vorticity layers ejecting off of wave crests. They also demonstrate that as the wave slope ( $ak$ ) is reduced, this signature is muted as airflow separations (and enhanced wind shear) become less frequent. As discussed earlier, the area integral of the mean wind shear is roughly proportional to the far field wind speed. Therefore, the reduced mean wind shear toward the surface (relative to the flat wall case) decreases the far field wind speed and the enhanced wind shear near the crest height increases the far field wind speed. Since the former contribution is more significant, the far field wind speed decreases and thus the equivalent surface roughness  $z_o$  increases due to the wave.

As the wave age increases to  $c/u_{*s} = 5.6$  and above, the enhancement of the wind shear almost completely disappears, indicating that little to no airflow separations are occurring. The decrease in wind shear toward the surface remains significant, but gradually decreases with increasing

$c/u_{*s}$ . Consequently, the reduction of far field wind speed and the increase of the equivalent surface roughness  $z_o$  are also less significant.

Note that the normalized mean shear remains slightly above the flat wall case (gray solid line) at the top of the domain ( $k\zeta = 4$ ) for the cases of  $c/u_{*s} = 5.6, 8.2, 11$ , suggesting that the wave effect on the mean shear has not completely disappeared at this height in these cases. If this slightly elevated wind shear persists further above, it is possible that the wind profiles approach closer to the solid gray line at higher elevations and  $z_o$  may be slightly lower than our estimates, which are made using the wind speed at  $k\zeta = 4$  (where the effects of the LES top boundary are small).

The mean normalized 3D TKE profiles are shown in Fig. 5e. For the two slow wave cases the enhancement of TKE is generally located at about the same elevation as the enhancement of the mean wind shear in Fig. 5c. As  $c/u_{*s}$  increases, this enhancement gradually diminishes and completely disappears at  $c/u_{*s} = 11$ . Although small deviations to the TKE profile are present closer to the surface, it becomes more uniform overall and suggests substantially reduced wave impacts.

Next, we examine the case for waves opposing wind. With slow waves at  $c/u_{*s} = -1.4$ , the wind speed and wind shear profiles (solid dark red lines, Figs. 5b,d) in the lower part of the wave boundary layer are quite similar to those for slow waves following wind at  $c/u_{*s} = 1.4$  (solid dark red lines, Figs. 5a, 4c), except that the height of the enhanced wind shear is slightly lower. However, they are significantly different in the upper region. For  $c/u_{*s} = 1.4$ , the wind shear converges to that over a flat surface above around  $k\zeta = 0.6$ , but with  $c/u_{*s} = -1.4$  the wind shear becomes significantly reduced above around  $k\zeta = 0.5$  before it converges to the flat wall case near  $k\zeta = 4$ . Consequently, the far field wind speed is more reduced and the equivalent roughness of  $z_o/z_{ob} = 7.04$  is significantly larger than that of  $c/u_{*s} = 1.4$ . The mean TKE profile at  $c/u_{*s} = -1.4$  is similar to that of  $c/u_{*s} = 1.4$  with its peak slightly above the height of the peak of the mean wind shear (Fig. 5f).

As the wave speed increases and  $c/u_{*s}$  decreases from  $-1.4$  to  $-11$ , the mean wind shear profile maintains a qualitatively similar character. The wind shear continues to show pronounced enhancement, but its peak shifts closer to the surface and slightly weakens with more negative  $c/u_{*s}$ . The pattern of reduced wind shear toward the surface slightly increases with faster waves but remains largely unchanged. Above the layer of enhancement, the wind shear reduces much more dramatically and expands much farther away from the surface as  $c/u_{*s}$  becomes more negative, suggesting that the vertical extent of the wave impact on mean wind shear increases with increasing wave speed. Cao et al. (2020) suggest that the increasingly strong vertical velocity interacts with the mean wind shear to amplify the effect of wave kinematics on the airflow fields as the opposing wave speed increases. Because of this elevated layer of reduced wind shear, the far field wind speed continues to decrease and the effective surface roughness  $z_o$  significantly increases as  $c/u_{*s}$  becomes more negative, reaching to  $z_o/z_{ob} = 31.80$  at  $c/u_{*s} = -11$ . The mean TKE profile also remains

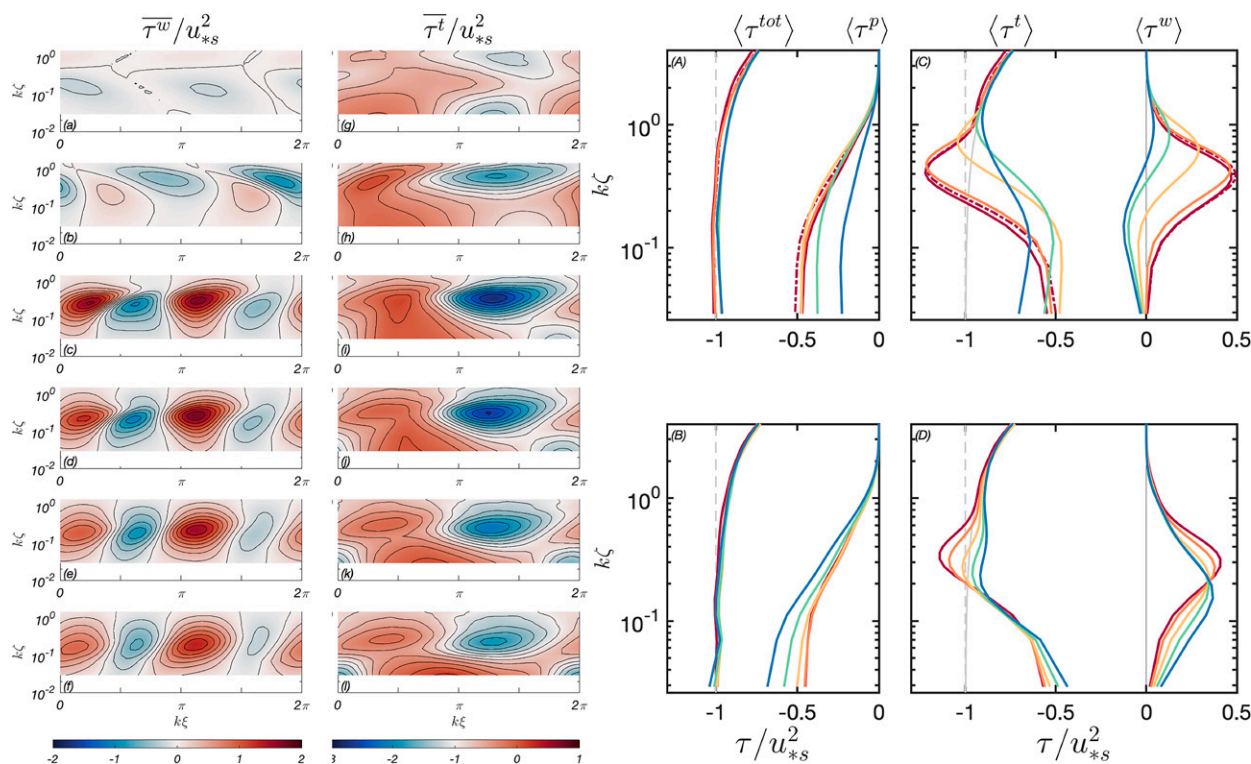


FIG. 6. (left) Normalized phase-averaged fields of wave-coherent stress ( $\overline{\tau^w}/u_{*s}^2 = \overline{\tilde{u}\tilde{W}}/u_{*s}^2$ ) and turbulent stress ( $\overline{\tau^t}/u_{*s}^2 = \overline{u'W'}/u_{*s}^2$ ) in the mapped  $\xi$ - $\zeta$  coordinate for (top three rows) waves following wind ( $c/u_{*s} = 11.0, 5.6, 1.4$ ) and (bottom three rows) waves opposing wind ( $c/u_{*s} = -1.4, -5.6, -11.0$ ). (right) Normalized vertical profiles of horizontally averaged momentum budget terms for (top) waves following wind and (bottom) waves opposing wind, including the total wind stress ( $\langle \tau^{tot} \rangle / u_{*s}^2$ ), pressure stress ( $\langle \tau^p \rangle / u_{*s}^2$ ), turbulent stress ( $\langle \tau^t \rangle / u_{*s}^2$ ), and wave-coherent stress ( $\langle \tau^w \rangle / u_{*s}^2$ ) for  $|c/u_{*s}| = 1.4, 2.8, 5.6, 8.2,$  and  $11.0$  (dark red, dark orange, light orange, light green, and blue). The dot-dashed dark red line is the Stokes wave case for  $c/u_{*s} = 1.4$ . Gray lines are profiles over a flat wall as explained in the main text.

qualitatively similar; the height of the well-defined TKE peak gradually decreases and the peak value slightly decreases as  $c/u_{*s}$  becomes more negative (Fig. 5f).

Similar to the case of faster waves following wind  $c/u_{*s} = 5.6, 8.2,$  and  $11$ , the wave effect on the mean wind shear has not completely disappeared at the top of the domain ( $k\zeta = 4$ ) for faster waves opposing wind ( $c/u_{*s} = -5.6, -8.2,$  and  $-11$ ). The wind shear is still below the flat wall case at this height (compared to the gray solid line). If the reduced wind shear persists further above, the wind profiles may deviate further from the solid gray line at higher elevations, which may result in a larger  $z_o$  than our estimates in Table 1.

### e. Momentum budget in mapped coordinate

The horizontally averaged momentum budget (or wind stress partition) as described in Eq. (7) is shown in Figs. 6A,C (upper panels) for  $c/u_{*s} = 1.4, 2.8, 5.6, 8.2,$  and  $11$  (increasing wave age transitioning from warmer to cooler colors) for waves following wind, and in Figs. 6B,D (lower panels) for  $c/u_{*s} = -1.4, -2.8, -5.6, -8.2,$  and  $-11$  (increasingly negative wave age transitioning from warmer to cooler colors) for waves opposing wind. Similar to the mean wind speed and

mean wind shear, the solid (dashed) gray lines represent linearly decreasing (constant) total wind stress in  $k\zeta$ . As discussed earlier, the horizontally averaged total stress  $\langle \tau^{tot} \rangle$ , which linearly decreases away from the surface, is equal to the sum of the pressure stress  $\langle \tau^p \rangle$ , the wave coherent stress  $\langle \tau^w \rangle = \langle \tilde{u}\tilde{W} \rangle$ , and the turbulent stress  $\langle \tau^t \rangle = \langle u'W' \rangle$  (including both resolved and SGS contributions in LES) in the wave boundary layer. Recall that  $W$  is a velocity normal to the mapped constant  $\zeta$  plane, so these stresses act normal to the wavy surface. The total stress  $\langle \tau^{tot} \rangle$  profiles shown in Figs. 6A,B are obtained by adding these three stress components calculated from the LES results, and are (almost) equal to the linearly decreasing stress profile (solid gray line, not visible). This convergence of  $\tau^{tot}$  confirms that the LES results properly satisfy the momentum budget.

The two-dimensional fields of the phase-averaged normalized turbulent stress  $\overline{\tau^t} = \overline{u'W'}$  and wave-coherent stress  $\overline{\tau^w} = \overline{\tilde{u}\tilde{W}}$  are displayed in mapped coordinates for  $c/u_{*s} = 11, 5.6,$  and  $1.4$  in Figs. 6a-c,g-i (upper panels) and for  $c/u_{*s} = -1.4, -5.6,$  and  $-11$  in Figs. 6d-f,j-l (lower panels). Note that the color scale of the turbulent stress is shifted such that red (blue) means the local turbulent stress is larger (smaller) than the normalized surface wind stress (which is  $-1$ ).

For the slow waves following wind ( $c/u_{*s} = 1.4$  and  $2.8$ ), the horizontally averaged wave coherent stress is significantly enhanced and positive (upward momentum flux) around the height where the mean wind shear and the TKE are also elevated. The two-dimensional distribution of the wave coherent stress  $\tilde{u}\tilde{W}$  (Fig. 6c) shows that intense upward momentum flux occurs just downstream of the crest where the high velocity fluid ( $\tilde{u} > 0$ ) is detached from the surface ( $\tilde{W} > 0$ ), and just downstream of the trough where the low velocity fluid ( $\tilde{u} < 0$ ) reattaches toward the surface ( $\tilde{W} < 0$ ). This suggests that the positive wave coherent stress is enhanced by intermittent airflow separation events. To compensate this elevated positive  $\langle \tau^w \rangle$ , the negative turbulent stress  $\langle \tau^t \rangle$  (downward momentum flux) is significantly enhanced at a similar elevation. This enhancement mainly occurs downstream of the trough (Fig. 6i). The magnitude of the negative pressure stress  $\langle \tau^p \rangle$  monotonically increases toward the surface and remains approximately constant at around  $-0.5$  below  $k\zeta = 0.1$  (Fig. 6A)—that is, the pressure stress (which is equal to the wave form drag at the surface) accounts for half of the total wind stress. The wave coherent stress  $\langle \tau^w \rangle$  becomes negligible below  $k\zeta = 0.05$  and the turbulent stress is reduced to about half of the wind stress and compensates for the large pressure stress nearer to the surface (Fig. 6C). For  $c/u_{*s} = 1.4$ , the addition of the Stokes solution to the wave shape enhances the pressure stress (and the form drag at the surface) by 9% above its sinusoidal counterpart.

As the wave age increases to  $c/u_{*s} = 5.6$  and above, the enhanced positive wave coherent stress rapidly diminishes and slightly moves upward (Fig. 6C). Near the surface the pressure stress still supports roughly half of the wind stress at  $c/u_{*s} = 5.6$  (Fig. 6A). As  $c/u_{*s}$  increases more, the magnitude of the pressure stress and the reduction of the turbulent stress gradually diminish but remain significant. At  $c/u_{*s} = 11$  the pressure stress still accounts for about 1/4 of the total wind stress.

For slow waves opposing wind at  $c/u_{*s} = -1.4$ , the vertical profiles of the stress components (Figs. 6B,D, dark red lines) are quite similar to those for the slow waves following wind at  $c/u_{*s} = 1.4$ , Figs. 6A,C, dark red lines). The positive enhancement of  $\langle \tau^w \rangle$  and the negative enhancement of  $\langle \tau^t \rangle$  are both apparent, but they are slightly weaker and occur at slightly lower elevations. These patterns are accompanied by significant  $\langle \tau^p \rangle$  (about 1/2 of the total wind stress) corresponding to the reduction of  $\langle \tau^t \rangle$  toward the surface, similar to the following case.

As the wave speed increases and  $c/u_{*s}$  decreases to  $-11$ , these patterns remain qualitatively similar, but the positive enhancement of  $\langle \tau^w \rangle$  and the negative enhancement of  $\langle \tau^t \rangle$  both gradually weaken and move lower in  $\zeta$ . This further confirms that the vertical extent of the strong wave perturbation is gradually suppressed as  $c/u_{*s}$  decreases. The pressure stress  $\langle \tau^p \rangle$  continues to increase near the surface, approaching almost 70% of the wind stress for  $c/u_{*s} = -11$ .

The two-dimensional fields of  $\tilde{\tau}$  and  $\tilde{\tau}^v$  for waves opposing wind (Figs. 6d–f, 5j–l) also show that the stress field for  $c/u_{*s} = -1.4$  remains qualitatively similar to  $c/u_{*s} = 1.4$ , and this pattern remains largely unchanged up to  $c/u_{*s} = -11$  with all

wave perturbations slowly weakening and migrating down as  $c/u_{*s}$  decreases. One notable development is the emergence of a region of positive  $\tilde{\tau} = \tilde{u}'\tilde{W}'$  just above the trough at  $c/u_{*s} = -5.6$  and  $-11$ , where the flow perturbation of enhanced negative  $\omega_y$  (wind shear) and reduced TKE have been observed earlier.

f. Energy budget and turbulence closure parameterization

We next investigate the energy budget inside the wave boundary layer. Hara and Sullivan (2015) have derived the equations governing the wave-fluctuation energy,  $E^w = (1/2)(\tilde{u}\tilde{u} + \tilde{w}\tilde{w})$ , and the turbulent kinetic energy,  $\bar{e} = (1/2)(\overline{u'u'} + \overline{v'v'} + \overline{w'w'})$ , in mapped coordinates. If the two governing equations are combined, averaged horizontally and normalized, the result yields

$$\left\langle \tilde{u} \frac{1}{J} \right\rangle \frac{\partial P}{\partial x} \frac{\kappa \zeta}{u_{*s}^3} + \frac{\partial \langle u \tilde{u} \rangle}{\partial \zeta} \frac{\kappa \zeta}{u_{*s}} - \frac{\partial (F^w + F^t)}{\partial \zeta} \frac{\kappa \zeta}{u_{*s}^3} - \left\langle \frac{1}{J} \epsilon \right\rangle \frac{\kappa \zeta}{u_{*s}^3} = 0, \tag{10}$$

where the second term is the shear production term, the third term is the transport term ( $F^w$  and  $F^t$  are the vertical transport of  $\epsilon^w$  and  $\bar{e}$ , respectively), and the fourth term is the viscous dissipation term. The first term arises because of the imposed pressure gradient (i.e., because the stress is not constant in vertical). Here,  $(F^w + F^t)$  at the surface is equal to the energy flux into the waves. Refer to Hara and Sullivan (2015) for more details on the derivation of the energy budget in mapped coordinates.

In Figs. 7a,b, the second, third, and fourth terms of Eq. (10) are plotted in solid, dot-dashed, and dotted lines with colors corresponding to their respective  $c/u_{*s}$ . The first term is approximately zero and shown as a solid gray line. Thin dotted lines near zero are equal to the sum of all the energy budget terms. Thin gray lines represent the mean shear production (mean wind shear) over a flat wall for linearly decreasing stress (solid) and constant stress (dashed) with respect to  $k\zeta$ . Note that the energy budget is not fully closed in the case of  $c/u_{*s} = -11$ . We suspect that this error arises in the calculation of the transport term and is caused by the increasingly strong pressure signal, but that the shear production and the dissipation terms are still reasonably accurate.

Previous modeling studies of the vertical mean wind profile and the drag coefficient over a surface wave train (or a spectrum of waves, i.e., many surface wave trains superimposed) have sought to close the turbulence in the wave boundary layer by parameterizing the eddy viscosity ( $K$ ) or the TKE dissipation rate ( $\langle \epsilon \rangle$ ) using the turbulent stress  $\langle \tau^t \rangle$  that varies with height due to the wave influence (e.g., Makin and Kudryavtsev 1999; Hara and Belcher 2004). Thus, one area of interest in the present study is to determine whether the character of the mean normalized wind shear (equivalent to the mean shear production term of the energy budget, solid lines in Figs. 7a,b and identical to Figs. 5c,d), the mean dissipation [last term in Eq. (10), dotted lines in Figs. 7a,b], and the mean turbulent stress share similarities in character over a range of wind-wave conditions. For this reason, we have included the profiles of the mean turbulent stress in Figs. 7c,d (previously

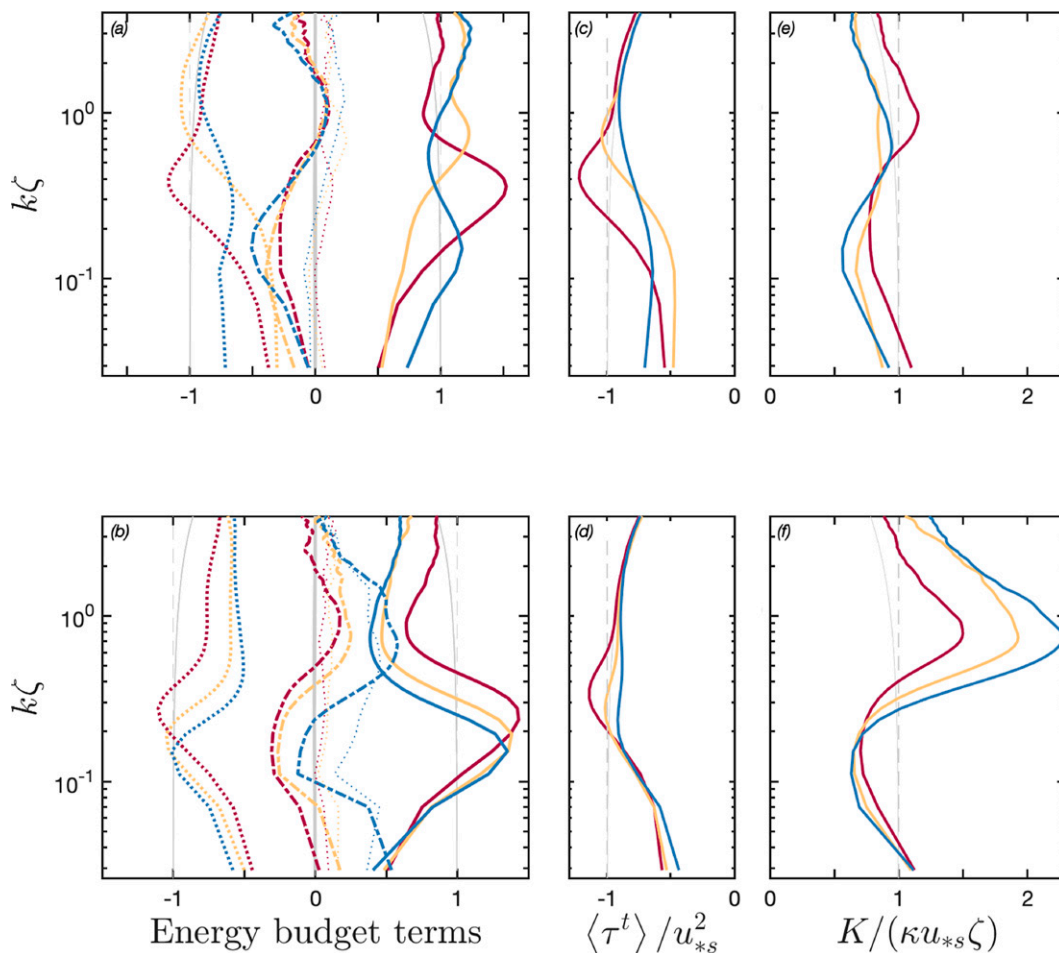


FIG. 7. (a),(b) Normalized vertical profiles of horizontally averaged energy budget terms. The first (pressure gradient), second (shear production), third (transport) and fourth (dissipation) terms of Eq. (10) are solid gray, solid, dot-dashed, and dotted lines, respectively, with thin dotted lines near zero equaling the sum of all energy budget terms. (c),(d) Normalized vertical profiles of horizontally averaged turbulent stress  $\langle \tau^t \rangle / u_{*s}^2$ , also shown in Fig. 6. (e),(f) Normalized vertical profiles of eddy viscosity  $[K / (\kappa u_{*s} \zeta)]$ . For the left, center, and right plots, the thin gray lines represent mean shear production, turbulent stress, and eddy viscosity profiles over a flat wall with linearly decreasing wind stress (solid) and constant stress (dashed) with respect to  $k\zeta$ . Results for waves following (opposing) wind are shown on the top (bottom) panel for  $|c/u_{*s}| = 1.4, 5.6$ , and  $11.0$  (dark red, light orange, and blue).

shown in Figs. 6C,D), and the profiles of the normalized eddy viscosity  $K / (\kappa u_{*s} \zeta)$  in Figs. 7e,f, where  $K = \langle \tau^t \rangle / (\partial \langle u \rangle / \partial \zeta)$ .

In all cases, the shear production roughly balances the viscous dissipation throughout the wave boundary layer, with a relatively modest contribution from the transport term (except for  $c/u_{*s} = -11$ ). The profiles of the shear production and viscous dissipation are reasonably correlated with the profile of the turbulent stress (Figs. 7c,d). All three profiles are significantly reduced near the surface for all  $c/u_{*s}$  cases, and enhanced further above in the cases of  $c/u_{*s} = 1.4, -1.4, -5.6, -11$ , although the enhancement of  $\langle \tau^t \rangle$  occurs somewhat above the enhancement of the shear production and the viscous dissipation in the cases of  $c/u_{*s} = -5.6$  and  $-11$ . This suggests that the existing turbulent closure model to parameterize  $\epsilon$  in terms of  $\langle \tau^t \rangle$  may be appropriate for a wide range of  $c/u_{*s}$ .

One notable exception to the generally good correlation between the dissipation rate and the turbulent stress is that for the cases of waves opposing wind, the shear production and viscous dissipation are both significantly reduced (by as much as 1/2) above  $k\zeta = 1$  all the way to the top ( $k\zeta = 4$ ), even if the turbulent stress  $\langle \tau^t \rangle$  is almost equal to the total wind stress  $\langle \tau^{\text{tot}} \rangle$  (i.e., the wave effect on the turbulent stress is negligible) in the same  $k\zeta$  range. As discussed earlier, this reduced mean wind shear makes a significant contribution to the enhancement of the equivalent roughness length  $z_o$  and the drag coefficient. A turbulence closure model based on the wave modified  $\langle \tau^t \rangle$  alone would completely miss this impact.

The profiles of the normalized eddy viscosity  $K / (\kappa u_{*s} \zeta)$  for waves following wind (Fig. 7e) show that they are not too far from the gray solid line throughout the wave boundary layer, but its variation is not well correlated with  $\langle \tau^t \rangle$ . For waves

opposing wind, the normalized eddy viscosity significantly increases roughly above  $k\zeta = 0.4$ , and this increase is totally uncorrelated with  $\langle \tau' \rangle$ . These observations suggest that parameterizing  $K$  inside the wave boundary layer in terms of  $\langle \tau' \rangle$  is problematic, particularly for waves opposing wind.

*g. Wave growth/decay rate and equivalent roughness length*

The normalized phase-dependent surface stress distribution is plotted in Figs. 2G,H for waves following wind, and in Figs. 2I,J for waves opposing wind. Since the total normal stress is a sum of the pressure and the turbulent normal stress, both the total normal stress (solid line) and the pressure stress alone (dotted line) are shown in Figs. 2G,I. The turbulent tangential surface stress is presented in Figs. 2H,J.

Both the normal stress in phase with the normal wave orbital velocity and the tangential stress in phase with the tangential wave orbital velocity contribute to the total energy flux (EF) into waves. The wave growth/decay rate  $\beta$  (which is positive/negative for wave growth/decay) is then calculated by dividing EF by the wave energy. We use the common expression of the wave growth/decay rate

$$\beta = c_\beta \left( \frac{u_{*s}}{c} \right)^2 \frac{\rho_a}{\rho_w} \omega, \quad (11)$$

where  $\omega$  is the wave frequency. The coefficient  $c_\beta$  is then evaluated based on the energy flux by the tangential turbulent stress only ( $c_{\beta t}$ ), by the normal turbulent stress only ( $c_{\beta n}$ ), by the pressure only ( $c_{\beta p}$ ), as well as based on the total energy flux ( $c_{\beta tot}$ ). The results are summarized in Table 1 and in Fig. 8a. For more details on how we compute each component of  $c_\beta$ , refer to Hara and Sullivan (2015) and Husain et al. (2019).

Consistent with Husain et al. (2019) for waves with  $c/u_{*s} = 1.4$ , the pressure field (as well as the total normal stress field) is strongly modified by wind flow over steep, strongly forced waves. In the dead zone above the leeward face of the wave (where wind velocity is weak), pressure remains almost zero before increasing to a maximum downstream of the trough on the windward face of the wave. The significant downstream phase shift of the pressure maximum from the trough is responsible for the large energy flux and a resulting  $c_{\beta tot}$  of 18.0 (note that only pressure modulation out of phase with wave surface elevation contributes to the energy flux). The addition of a nonlinear Stokes solution to the bottom wave shape slightly increases  $c_{\beta tot}$  to 18.2 (see black squares in Fig. 8a). With increasing  $c/u_{*s}$ , the magnitude of the pressure (and the total normal stress) variation and the resulting energy flux to waves rapidly decrease, and consequently  $c_{\beta tot}$  decreases to 3.9 at  $c/u_{*s} = 11$  (see thick solid black line in Fig. 8a).

For waves opposing wind, as  $c/u_{*s}$  becomes more negative the pressure perturbation becomes stronger and more in phase with  $-h$  (negative wave elevation) due to the increasing relative wind velocity  $\langle (u) - c \rangle$ , as discussed in section 3a (note the difference in vertical scale between Figs. 2G,I). Nevertheless, a significant pressure component out of phase with  $-h$  exists (buried in the strong in-phase component) and its contribution to the negative energy flux and the wave

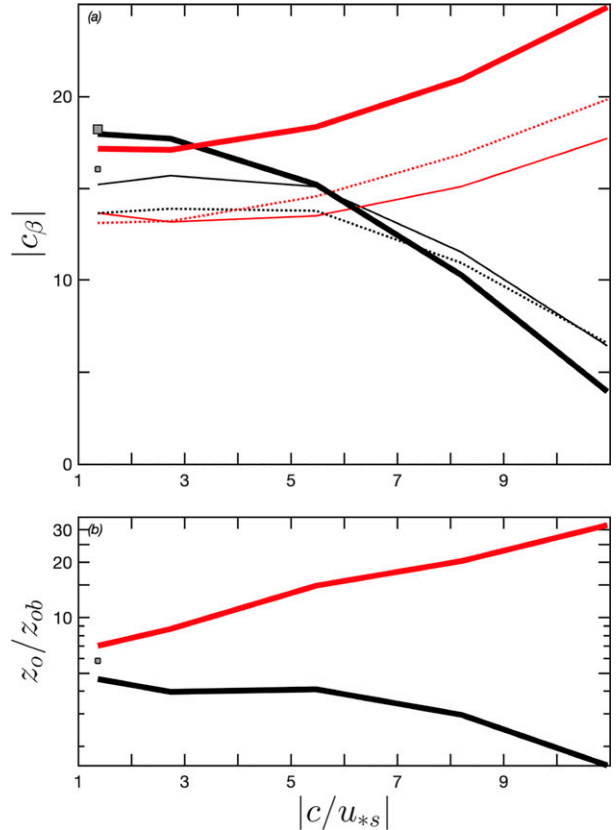


FIG. 8. (top) Wave growth/decay coefficient  $|c_\beta|$  for waves following wind (black lines) and for waves opposing wind (red lines) as a function of  $|c/u_{*s}|$ . Thin solid lines represent the contribution of the total normal stress ( $c_{\beta p} + c_{\beta n}$ ), dotted lines represent the pressure contribution ( $c_{\beta p}$ ), and thick solid lines represent the sum of all components ( $c_{\beta tot} = c_{\beta p} + c_{\beta n} + c_{\beta t}$ ). (bottom) Ratio of the equivalent surface roughness to the background (parameterized) surface roughness  $z_0/z_{ob}$  as a function of  $|c/u_{*s}|$  for waves following wind (black line) and waves opposing wind (red line). In both plots, the dark gray squares represent the Stokes wave case for  $c/u_{*s} = 1.4$  for  $c_{\beta tot}$  (large square) and  $c_{\beta p}$  only (small square).

decay rate significantly increases with increasingly negative  $c/u_{*s}$ .

At  $c/u_{*s} = -1.4$  the magnitude of  $c_{\beta tot} = -17.2$  is close to the magnitude of  $c_{\beta tot} = 18.0$  at  $c/u_{*s} = 1.4$ . Therefore, while the direction of energy flux reverses between these two cases, its magnitude is similar. The magnitude of  $c_{\beta p}$ , which is proportional to the pressure form drag, is also similar between the two cases. Recall that the momentum flux is downward in both cases even if the energy flux is downward/upward with waves following/opposing wind. As wave speed increases and  $c/u_{*s}$  decreases to  $-11$ ,  $c_{\beta tot}$  significantly decreases to  $-24.9$  (Fig. 8a).

In Fig. 9, our estimated  $c_{\beta tot}$  and  $c_{\beta p}$  values (Fig. 9a) and  $\beta/\omega$  values (Figs. 9b,c) for waves opposing wind are compared to the previous LES study of Cao et al. (2020) as well as the results of Harris et al. (1995), Cohen (1997), Donelan (1999), Peirson et al. (2003), and Mitsuyasu and Yoshida (2005).

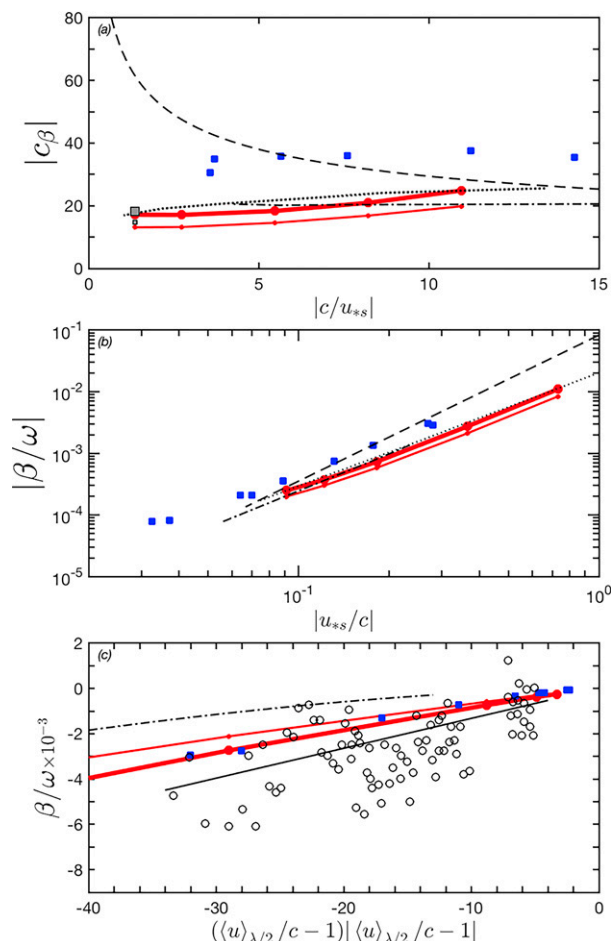


FIG. 9. (top) Comparison of wave decay coefficient  $|c_\beta|$  as a function of wave age  $|c/u_{*s}|$  for the current LES study (thick red line: total  $c_{\beta tot}$ , thin red line: only  $c_{\beta pp}$ ), the wall-resolved LES results of Cao et al. (2020) (blue squares), the parameterization of Mitsuyasu and Yoshida (2005) (dashed line), and the results of Harris et al. (1995) (dot-dashed line) and Cohen (1997) (dotted line). (middle) Comparison of wave decay rate  $|\beta/\omega|$  as a function of inverse wave age  $|u_{*s}/c|$  with lines corresponding to those of the top plot. Compare with Cao et al. (2020, their Fig. 18). (bottom) Comparison of wave decay rate  $\beta/\omega$  as a function of  $((u_{\lambda/2}/c - 1)|u_{\lambda/2}/c - 1|)$ , including the current LES results (thick red line: total decay rate, thin red line: pressure contribution only), the wall-resolved LES of Cao et al. (2020) (blue squares), the parameterization of Mitsuyasu and Yoshida (2005) (dot-dashed line), and the observational results and parameterization of Donelan (1999) (black circles and black line, respectively). Compare to Fig. 19 of Cao et al. (2020).

Since most previous studies focused on wave attenuation due to pressure only, they should be compared with our results for  $c_{\beta pp}$  or corresponding  $\beta/\omega$  (thin red lines).

Our results, plotted against  $|c/u_{*s}|$  or  $|u_{*s}/c|$ , are near the lower end of the other studies (Figs. 9a,b). In particular, the results of Cao et al. (2020) (the only other LES study) are consistently larger than ours by a factor of around 2. The differences we do see may be due to our choice of a rather steep wave slope  $ak = 0.27$  compared to  $ak = 0.08$ – $0.15$  used in Cao

et al. (2020). Such a difference is not surprising since it has been well accepted that the growth rate of waves following wind may vary significantly depending on the wave slope and other wind and wave characteristics. When we plot the decay rate as a function of  $(\langle u \rangle_{\lambda/2}/c - 1)|\langle u \rangle_{\lambda/2}/c - 1|$  (Fig. 9c), our results appear to be closer to those of Cao et al. (2020, see their Fig. 19) and are quite consistent with the observations and the parameterization of Donelan (1999, see their Fig. 4).

In Fig. 8b we summarize the estimated values for  $z_o/z_{ob}$ , which represents the enhancement of the effective roughness length  $z_o$  due to resolved waves relative to the background roughness length  $z_{ob}$ . The results of  $z_o/z_{ob}$  are shown in a log scale because the increasing wind speed above the wave boundary layer due to resolved waves is proportional to  $\log(z_o/z_{ob})$ . The figure highlights the strong dependence of the effective roughness length and the drag coefficient on  $c/u_{*s}$ . The enhancement rapidly decreases as  $c/u_{*s}$  increases with waves following wind. However, with waves opposing wind, it rapidly increases with increasingly negative  $c/u_{*s}$ ; that is, faster waves opposing wind have the largest impact on the drag coefficient. As discussed earlier, the wave nonlinearity modifies  $z_o/z_{ob}$  by about 25% (from the black solid line to the small gray square), which is not large but is still a significant effect. Such impacts are likely present in other wind-wave conditions; that is, our overall results likely contain a minimum 25% uncertainty attributable to wave nonlinearity.

It is interesting that while the magnitude of  $c_{\beta pp}$  is similar (i.e., the pressure form drag is similar) between the cases of  $c/u_{*s} = 1.4$  and  $-1.4$ , the wave enhanced effective roughness length  $z_o/z_{ob}$  is significantly larger for waves opposing wind. This suggests that the increase in the effective roughness (drag coefficient) is not necessarily caused by an increase in the wave form drag. This difference in behavior of  $c_{\beta pp}$  and  $z_o/z_{ob}$  can be explained based on the energy budget inside the wave boundary layer.

Hara and Belcher (2004) show that inside the constant stress layer the downward energy flux at the top of the wave boundary layer is roughly equal to the mean wind speed multiplied by the wind stress  $\bar{u}\tau_s$  because the vertical TKE transport is small there. They then show that this energy input at the top is equal to the sum of the viscous dissipation (integrated over the entire wave boundary layer) and the energy output (energy flux into surface waves) at the bottom. Therefore, with a fixed wind stress (as in the current study), the wind speed at the top and the effective surface roughness (or the drag coefficient) are determined by a sum of the integrated viscous dissipation and the energy flux to waves.

Hara and Belcher (2004) then assume that the reduction of the viscous dissipation inside the wave boundary layer (compared to that over a flat surface) is correlated with the reduction of the turbulent stress, which is caused by the pressure form drag. Therefore, if the pressure form drag is similar between the cases of  $c/u_{*s} = 1.4$  and  $c/u_{*s} = -1.4$ , we would expect that the reduction of the turbulent stress and the reduction of the viscous dissipation are similar as well. However, the energy flux into surface waves (energy output from the wave boundary layer at the bottom) is positive (negative) for waves following (opposing) wind. Therefore, even if the

integrated viscous dissipation is similar, the energy input at the top of the wave boundary layer must be larger (smaller) for waves following (opposing) wind. Consequently, the wind speed near the top of the wave boundary layer must be larger (smaller) and the drag coefficient and effective roughness length must be smaller (larger) for waves following (opposing) wind. Put succinctly, the reversal of the energy flux direction to/from waves may explain why  $z_o/z_{ob}$  is significantly larger for waves opposing wind.

In fact, a quick estimate of the difference in the far field wind speed  $\langle u \rangle / u_{*s}$  due to the reversal of the energy flux alone (estimate made using the  $c_{\beta\text{tot}}$  values in Table 1) is about 1.3, which is roughly consistent with the observed difference of 1.7 at  $k\zeta = 4$  (roughly the height of the wave boundary layer) in our LES results. This indicates that the increase of the equivalent roughness from  $c/u_{*s} = 1.4$  to  $c/u_{*s} = -1.4$  is mainly attributed to the reversal of the energy flux. Our LES results therefore suggest that it is important to account for the effect of energy flux to/from surface waves (in addition to the wave form drag) when estimating the wave modified effective roughness length  $z_o$  and the drag coefficient, particularly when waves oppose the wind.

#### 4. Summary

In this study, we use large-eddy simulation (LES) to simulate turbulent wind flow over steep waves ( $ak = 0.27$ ) following and opposing the wind for a range of wave speeds relative to wind forcing ( $|c/u_{*s}| = 1.4, 2.8, 5.6, 8.2, \text{ and } 11$ ). Our results show that the phase averaged wind flow patterns over slow waves following wind  $c/u_{*s} = 1.4$  are strongly influenced by intermittent but frequent airflow separations, characterized by enhanced spanwise vorticity detached from the leeward crest. The winds weaken and recirculate in the trough of the wave. Inside the dead zone below the detached enhanced vorticity layer, the TKE, viscous dissipation, and vorticity are all significantly reduced (Figs. 3c,i,o,C,I,O). Flow separation alters the mean wind profile (Fig. 5) and induces shifts in the pressure field such that the wind stress partition (including form drag, Fig. 6) and wave growth rate (Fig. 8) are modified significantly. As wave age increases, the frequency of intermittent airflow separation events and their signature in the phase-averaged flow fields rapidly diminishes.

Wind flow over opposing waves results in a strong wave-induced flow perturbation that intensifies and is compressed near the surface as the phase speed of the waves increases. We observe a number of phase-averaged flow features similar to those over slow waves following wind, e.g., enhanced TKE, dissipation, and detached vorticity near the wave crest, as well as reduced TKE, dissipation, and vorticity in the wave trough below the detached enhanced vorticity layer (Figs. 3D–F,J–L,P–R). However, the strong positive wind along the wave shape over opposing waves (in a frame of reference moving with the wave) inhibits apparent separation-like flow patterns. Increases in opposing wave speed intensify the in-phase component of the pressure field (Figs. 2d–f,D–F,I) and make the flow appear to follow the

potential wave theory. They also induce a significant out-of-phase component of the pressure field responsible for an increase in the effective surface roughness and wave decay rate (Fig. 8). Our estimated wave decay rates are consistent with those of previous studies, including a recent study using wall-resolved LES (Cao et al. 2020), model studies using RANS solutions (Al-Zanaidi and Hui 1984; Harris et al. 1995; Mastenbroek 1996; Cohen 1997), and laboratory studies (Donelan 1999; Peirson et al. 2003; Mitsuyasu and Yoshida 2005).

It is noteworthy that the observed separation-like signatures of wind over the wave crest are qualitatively similar to flow separations of wind blowing over a rotating cylinder (placed horizontally with its axis perpendicular to the wind), which were investigated by Gad-el Hak and Bushnell (1991) and Degani et al. (1998). This is not surprising because the wind velocity at the wave crest is not zero but positive (negative) for waves opposing (following) wind in a reference frame moving with the wave, and the wind velocity at the top of the rotating cylinder is also positive (negative) if the cylinder rotates forward (backward). Gad-el Hak and Bushnell (1991) notes that there is a close relationship between steady flow over a moving wall and unsteady flow over a fixed wall, and that in these conditions separation points may be lifted above the surface and the traditional criterion of zero surface shear stress does not apply. In fact, they predict that near-surface wind shear becomes negative (positive) over a cylinder rotating forward (backward), which corresponds to a crest of waves opposing (following) wind. This prediction is consistent with our LES results discussed earlier; in particular, producing strong negative vorticity in the trough for faster waves (Figs. 3P–R; also see Fig. 1 in Degani et al. 1998).

Our estimates of the equivalent surface roughness  $z_o$  (including the effect of resolved waves) relative to the background roughness  $z_{ob}$  (representing the form drag of unresolved waves and viscosity) show that the enhancement  $z_o/z_{ob}$  is significant for slow waves following wind but decreases as the wave age increases. On the other hand, for waves opposing wind,  $z_o/z_{ob}$  rapidly increases as the wave speed increases. By comparing the results of the slowest waves for both following and opposing wind ( $c/u_{*s} = 1.4$  and  $-1.4$ ), we find that the pressure form drag is very similar but  $z_o/z_{ob}$  is significantly larger with waves opposing wind, suggesting that the increase of equivalent roughness length (or drag coefficient) is not necessarily caused by an increase of the wave form drag. We refer to the study of Hara and Belcher (2004) and speculate that the reversal of energy flux direction from wind to waves (from waves to wind) for waves following (opposing) wind is responsible for the difference in  $z_o/z_{ob}$ . This finding suggests that it is important to account for the reversed energy flux when estimating the enhancement of the effective surface roughness due to opposing waves.

Waves opposing wind often appear when the wind field rapidly changes in space and/or time, a situation commonly encountered under tropical cyclones. Previous modeling efforts of the sea-state-dependent drag coefficient have

predicted waves opposing wind may significantly enhance the drag coefficient in such conditions because of the assumed large form drag (Reichl et al. 2014; Chen and Curcic 2016; Chen et al. 2020). Results from the present study provide credible support for such modeling efforts. In addition, our energy budget analysis (section 3f) and the discussion on the roughness length (section 3g) identify the strengths and weaknesses of existing models of mean wind profile and drag coefficient over a spectrum of waves.

In this study we do not propose a new parameterization of the drag coefficient as a function of wave age or other simple wave parameters. This is mainly because the total wind stress is expected to be dependent on integration of the wave form drag due to waves of all scales and directions (e.g., Donelan et al. 2012; Reichl et al. 2014). Only when the entire wave spectrum can be characterized by simple wave parameters (e.g., fetch-dependent growing wind seas under steady uniform wind) can a simple drag coefficient parameterization be feasible. Since waves opposing wind appear when the wind field rapidly changes in space/time, it is unlikely that a simple drag coefficient parameterization is applicable in such conditions. Instead, the aim of this study is to advance our understanding of how waves opposing wind interact with wind, how large the wave decay rate and the wave form drag are, and how the mean wind profile is modified by such waves.

Previous studies suggest that the wave growth/decay rate and the effective roughness length may be significantly modified by sea spray (e.g., Bell et al. 2012; Innocentini and Goncalves 2010). In addition, they may be further modified by the nonlinearity of surface waves (e.g., Zdyski and Feddersen 2020). In this study the spray effects have not been addressed and the wave nonlinearity effect has been investigated by one simulation only using the second-order Stokes waves. It is certainly desirable to incorporate these effects more fully in future LES studies, particularly because waves opposing wind are common under tropical cyclones, and spray and nonlinear effects may dominate in such high wind conditions. However, there are many conditions where our results are more likely relevant. For example, even under a tropical cyclone there is a large area (away from the eyewall) where wind speed is modest and opposing dominant swell waves are not very steep, with  $|c/u_{*s}|$  as low as 5–10 (Chen et al. 2020). In such conditions, the results from this study are likely beneficial for improving the sea-state-dependent wind stress parameterization.

*Acknowledgments.* We acknowledge support of the National Science Foundation (Physical Oceanography) Grant OCE-1458984 (URI). We also acknowledge high-performance computing support from Yellowstone and Cheyenne (doi:10.5065/D6RX99HX) provided by NCAR's Computational and Information Systems Laboratory, sponsored by the National Science Foundation.

*Data availability statement.* All large-eddy simulation data created and used during this study are openly available at <http://dx.doi.org/10.17632/8vj68sr4rx.1>.

## REFERENCES

- Åkervik, E., and M. Vartdal, 2019: The role of wave kinematics in turbulent flow over waves. *J. Fluid Mech.*, **880**, 890–915, <https://doi.org/10.1017/jfm.2019.708>.
- Al-Zanaidi, M. A., and W. H. Hui, 1984: Turbulent airflow over water waves—a numerical study. *J. Fluid Mech.*, **148**, 225–246, <https://doi.org/10.1017/S0022112084002329>.
- Andreas, E. L., 2004: Spray stress revisited. *J. Phys. Oceanogr.*, **34**, 1429–1440, [https://doi.org/10.1175/1520-0485\(2004\)034<1429:SSR>2.0.CO;2](https://doi.org/10.1175/1520-0485(2004)034<1429:SSR>2.0.CO;2).
- Ardhuin, F., T. H. C. Herbers, K. P. Watts, G. P. van Vledder, R. Jensen, and H. C. Graber, 2007: Swell and slanting-fetch effects on wind wave growth. *J. Phys. Oceanogr.*, **37**, 908–931, <https://doi.org/10.1175/JPO3039.1>.
- Banner, M. L., 1990: The influence of wave breaking on the surface pressure distribution in wind–wave interactions. *J. Fluid Mech.*, **211**, 463–495, <https://doi.org/10.1017/S0022112090001653>.
- , and W. K. Melville, 1976: On the separation of air flow over water waves. *J. Fluid Mech.*, **77**, 825–842, <https://doi.org/10.1017/S0022112076002905>.
- Belcher, S. E., and J. C. R. Hunt, 1993: Turbulent shear flow over slowly moving waves. *J. Fluid Mech.*, **251**, 109, <https://doi.org/10.1017/S0022112093003350>.
- , and —, 1998: Turbulent flow over hills and waves. *Annu. Rev. Fluid Mech.*, **30**, 507–538, <https://doi.org/10.1146/annurev.fluid.30.1.507>.
- , T. M. J. Newley, and J. C. R. Hunt, 1993: The drag on an undulating surface induced by the flow of a turbulent boundary layer. *J. Fluid Mech.*, **249**, 557–596, <https://doi.org/10.1017/S0022112093001296>.
- Bell, M. M., M. T. Montgomery, and K. A. Emanuel, 2012: Air–sea enthalpy and momentum exchange at major hurricane wind speeds observed during CBLAST. *J. Atmos. Sci.*, **69**, 3197–3222, <https://doi.org/10.1175/JAS-D-11-0276.1>.
- Black, P. G., and Coauthors, 2007: Air–sea exchange in hurricanes: Synthesis of observations from the coupled boundary layer air–sea transfer experiment. *Bull. Amer. Meteor. Soc.*, **88**, 357–374, <https://doi.org/10.1175/BAMS-88-3-357>.
- Bourassa, M. A., D. G. Vincent, and W. L. Wood, 1999: A flux parameterization including the effects of capillary waves and sea state. *J. Atmos. Sci.*, **56**, 1123–1139, [https://doi.org/10.1175/1520-0469\(1999\)056<1123:AFPITE>2.0.CO;2](https://doi.org/10.1175/1520-0469(1999)056<1123:AFPITE>2.0.CO;2).
- Buckley, M. P., and F. Veron, 2016: Structure of the airflow above surface waves. *J. Phys. Oceanogr.*, **46**, 1377–1397, <https://doi.org/10.1175/JPO-D-15-0135.1>.
- , and —, 2019: The turbulent airflow over wind generated surface waves. *Eur. J. Mech.*, **73B**, 132–143, <https://doi.org/10.1016/j.euromechflu.2018.04.003>.
- Cao, T., and L. Shen, 2021: A numerical and theoretical study of wind over fast-propagating water waves. *J. Fluid Mech.*, **919**, A38, <https://doi.org/10.1017/jfm.2021.416>.
- , B.-Q. Deng, and L. Shen, 2020: A simulation-based mechanistic study of turbulent wind blowing over opposing water waves. *J. Fluid Mech.*, **901**, A07, <https://doi.org/10.1017/jfm.2020.591>.
- Chalikov, D., and S. Rainchik, 2011: Coupled numerical modelling of wind and waves and the theory of the wave boundary layer. *Bound.-Layer Meteor.*, **138**, 1–41, <https://doi.org/10.1007/s10546-010-9543-7>.
- Chen, S. S., and M. Curcic, 2016: Ocean surface waves in Hurricane Ike (2008) and Superstorm Sandy (2012): Coupled

- model predictions and observations. *Ocean Modell.*, **103**, 161–176, <https://doi.org/10.1016/j.ocemod.2015.08.005>.
- Chen, X., I. Ginis, and T. Hara, 2020: Impact of shoaling ocean surface waves on wind stress and drag coefficient in coastal waters: 2. Tropical cyclones. *J. Geophys. Res. Oceans*, **125**, e2020JC016223, <https://doi.org/10.1029/2020JC016223>.
- Cohen, J. E., 1997: Theory of turbulent wind over fast and slow waves. Ph.D. thesis, University of Cambridge, 228 pp., <https://doi.org/10.17863/CAM.31086>.
- Cronin, M. F., and Coauthors, 2019: Air-sea fluxes with a focus on heat and momentum. *Front. Mar. Sci.*, **6**, 430, <https://doi.org/10.3389/fmars.2019.00430>.
- Degani, A. T., J. D. A. Walker, and F. T. Smith, 1998: Unsteady separation past moving surfaces. *J. Fluid Mech.*, **375**, 1–38, <https://doi.org/10.1017/S0022112098001839>.
- Deike, L., and W. K. Melville, 2018: Gas transfer by breaking waves. *Geophys. Res. Lett.*, **45**, 10482–10492, <https://doi.org/10.1029/2018GL078758>.
- , L. Lenain, and W. K. Melville, 2017: Air entrainment by breaking waves. *Geophys. Res. Lett.*, **44**, 3779–3787, <https://doi.org/10.1002/2017GL072883>.
- Donelan, M. A., 1999: Wind-induced growth and attenuation of laboratory waves. *Wind-over-Wave Couplings: Perspectives and Prospects*, S. G. Sajjadi, N. H. Thomas, and J. C. R. Hunt, Eds., Clarendon, 183–194.
- , 2004: On the limiting aerodynamic roughness of the ocean in very strong winds. *Geophys. Res. Lett.*, **31**, L18306, <https://doi.org/10.1029/2004GL019460>.
- , F. W. Dobson, S. D. Smith, and R. J. Anderson, 1993: On the dependence of sea surface roughness on wave development. *J. Phys. Oceanogr.*, **23**, 2143–2149, [https://doi.org/10.1175/1520-0485\(1993\)023<2143:OTDOSS>2.0.CO;2](https://doi.org/10.1175/1520-0485(1993)023<2143:OTDOSS>2.0.CO;2).
- , A. V. Babanin, I. R. Young, and M. L. Banner, 2006: Wave-follower field measurements of the wind-input spectral function. Part II: Parameterization of the wind input. *J. Phys. Oceanogr.*, **36**, 1672–1689, <https://doi.org/10.1175/JPO2933.1>.
- , M. Curcic, S. S. Chen, and A. K. Magnusson, 2012: Modeling waves and wind stress. *J. Geophys. Res.*, **117**, C00J23, <https://doi.org/10.1029/2011JC007787>.
- Druzhinin, O. A., Y. I. Troitskaya, and S. S. Zilitinkevich, 2012: Direct numerical simulation of a turbulent wind over a wavy water surface. *J. Geophys. Res.*, **117**, C00J05, <https://doi.org/10.1029/2011JC007789>.
- Edson, J. B., and C. W. Fairall, 1998: Similarity relationships in the marine atmospheric surface layer for terms in the TKE and scalar variance budgets. *J. Atmos. Sci.*, **55**, 2311–2328, [https://doi.org/10.1175/1520-0469\(1998\)055<2311:SRITMA>2.0.CO;2](https://doi.org/10.1175/1520-0469(1998)055<2311:SRITMA>2.0.CO;2).
- , and Coauthors, 2013: On the exchange of momentum over the open ocean. *J. Phys. Oceanogr.*, **43**, 1589–1610, <https://doi.org/10.1175/JPO-D-12-0173.1>.
- Fairall, C. W., E. F. Bradley, J. E. Hare, A. A. Grachev, and J. B. Edson, 2003: Bulk parameterization of air-sea fluxes: Updates and verification for the COARE algorithm. *J. Climate*, **16**, 571–591, [https://doi.org/10.1175/1520-0442\(2003\)016<0571:BPOASF>2.0.CO;2](https://doi.org/10.1175/1520-0442(2003)016<0571:BPOASF>2.0.CO;2).
- Fan, Y., I. Ginis, T. Hara, C. W. Wright, and E. J. Walsh, 2009: Numerical simulations and observations of surface wave fields under an extreme tropical cyclone. *J. Phys. Oceanogr.*, **39**, 2097–2116, <https://doi.org/10.1175/2009JPO4224.1>.
- Gad-el Hak, M., and D. M. Bushnell, 1991: Separation control. *J. Fluids Eng.*, **113**, 5–30, <https://doi.org/10.1115/1.2926497>.
- Gent, P. R., 1977: A numerical model of the air flow above water waves. Part 2. *J. Fluid Mech.*, **82**, 349–369, <https://doi.org/10.1017/S0022112077000706>.
- , and P. A. Taylor, 1976: A numerical model of the air flow above water waves. *J. Fluid Mech.*, **77**, 105–128, <https://doi.org/10.1017/S0022112076001158>.
- Grachev, A. A., C. W. Fairall, J. E. Hare, J. B. Edson, and S. D. Miller, 2003: Wind stress vector over ocean waves. *J. Phys. Oceanogr.*, **33**, 2408–2429, [https://doi.org/10.1175/1520-0485\(2003\)033<2408:WSV0OW>2.0.CO;2](https://doi.org/10.1175/1520-0485(2003)033<2408:WSV0OW>2.0.CO;2).
- Grare, L., W. L. Peirson, H. Branger, J. W. Walker, J.-P. Giovanangeli, and V. Makin, 2013: Growth and dissipation of wind-forced, deep-water waves. *J. Fluid Mech.*, **722**, 5–50, <https://doi.org/10.1017/jfm.2013.88>.
- Hao, X., and L. Shen, 2019: Wind-wave coupling study using LES of wind and phase-resolved simulation of nonlinear waves. *J. Fluid Mech.*, **874**, 391–425, <https://doi.org/10.1017/jfm.2019.444>.
- Hara, T., and S. E. Belcher, 2002: Wind forcing in the equilibrium range of wind-wave spectra. *J. Fluid Mech.*, **470**, 223–245, <https://doi.org/10.1017/S0022112002001945>.
- , and —, 2004: Wind profile and drag coefficient over mature ocean surface wave spectra. *J. Phys. Oceanogr.*, **34**, 2345–2358, <https://doi.org/10.1175/JPO2633.1>.
- , and P. Sullivan, 2015: Wave boundary layer turbulence over surface waves in a strongly forced condition. *J. Phys. Oceanogr.*, **45**, 868–883, <https://doi.org/10.1175/JPO-D-14-0116.1>.
- Harris, J., I. Fultion, and R. Street, 1995: Decay of waves in an adverse wind. *Proceedings of the Sixth Asian Congress of Fluid Mechanics*, Y. Chew and C. Tso, Eds., Nanyang Technological University, 224–227.
- Hasselmann, D., and J. Bösenberg, 1991: Field measurements of wave-induced pressure over wind-sea and swell. *J. Fluid Mech.*, **230**, 391–428, <https://doi.org/10.1017/S0022112091000848>.
- Holthuijsen, L. H., M. D. Powell, and J. D. Pietrzak, 2012: Wind and waves in extreme hurricanes. *J. Geophys. Res.*, **117**, C09003, <https://doi.org/10.1029/2012JC007983>.
- Husain, N. T., T. Hara, M. P. Buckley, K. Yousefi, F. Veron, and P. P. Sullivan, 2019: Boundary layer turbulence over surface waves in a strongly forced condition: LES and observation. *J. Phys. Oceanogr.*, **49**, 1997–2015, <https://doi.org/10.1175/JPO-D-19-0070.1>.
- , —, and P. P. Sullivan, 2021: Wind turbulence over misaligned surface waves and air-sea momentum flux. Part II: Waves in oblique wind. *J. Phys. Oceanogr.*, **52**, 141–159, <https://doi.org/10.1175/JPO-D-21-0044.1>.
- Innocentini, V., and I. A. Goncalves, 2010: A simple spume droplets and wave stress parameterizations to study the impact on maritime near-surface variables. *Geophysical Research Abstracts*, Vol. 12, Abstract EGU2010-14701, <https://meetingorganizer.copernicus.org/EGU2010/EGU2010-14701.pdf>.
- Jiang, Q., P. P. Sullivan, S. Wang, J. Doyle, and L. Vincent, 2016: Impact of swell on air-sea momentum flux and marine boundary layer under low-wind conditions. *J. Atmos. Sci.*, **73**, 2683–2697, <https://doi.org/10.1175/JAS-D-15-0200.1>.
- Kudryavtsev, V. N., and V. K. Makin, 2001: The impact of air-flow separation on the drag of the sea surface. *Bound.-Layer Meteor.*, **98**, 155–171, <https://doi.org/10.1023/A:1018719917275>.
- , and —, 2002: Coupled dynamics of short waves and the airflow over long surface waves. *J. Geophys. Res.*, **107**, 3209, <https://doi.org/10.1029/2001JC001251>.

- , and —, 2004: Impact of swell on the marine atmospheric boundary layer. *J. Phys. Oceanogr.*, **34**, 934–949, [https://doi.org/10.1175/1520-0485\(2004\)034<0934:IOSOTM>2.0.CO;2](https://doi.org/10.1175/1520-0485(2004)034<0934:IOSOTM>2.0.CO;2).
- , and —, 2011: Impact of ocean spray on the dynamics of the marine atmospheric boundary layer. *Bound.-Layer Meteor.*, **140**, 383–410, <https://doi.org/10.1007/s10546-011-9624-2>.
- Kukulka, T., and T. Hara, 2008: The effect of breaking waves on a coupled model of wind and ocean surface waves. Part II: Growing seas. *J. Phys. Oceanogr.*, **38**, 2164–2184, <https://doi.org/10.1175/2008JPO3962.1>.
- , —, and S. E. Belcher, 2007: A model of the air–sea momentum flux and breaking-wave distribution for strongly forced wind waves. *J. Phys. Oceanogr.*, **37**, 1811–1828, <https://doi.org/10.1175/JPO3084.1>.
- Large, W. G., and S. Pond, 1981: Open ocean momentum flux measurements in moderate to strong winds. *J. Phys. Oceanogr.*, **11**, 324–336, [https://doi.org/10.1175/1520-0485\(1981\)011<0324:OOMFMI>2.0.CO;2](https://doi.org/10.1175/1520-0485(1981)011<0324:OOMFMI>2.0.CO;2).
- Liu, Y., D. Yang, X. Guo, and L. Shen, 2010: Numerical study of pressure forcing of wind on dynamically evolving water waves. *Phys. Fluids*, **22**, 041704, <https://doi.org/10.1063/1.3414832>.
- Makin, V. K., and V. N. Kudryavtsev, 1999: Coupled sea surface-atmosphere model: 1. Wind over waves coupling. *J. Geophys. Res.*, **104**, 7613–7623, <https://doi.org/10.1029/1999JC900006>.
- , and —, 2002: Impact of dominant waves on sea drag. *Bound.-Layer Meteor.*, **103**, 83–99, <https://doi.org/10.1023/A:1014591222717>.
- Mastenbroek, C., 1996: Wind-wave interaction. Ph.D. thesis, Delft Technical University, 119 pp., <http://resolver.tudelft.nl/uuid:b91093af-ccae-4d85-894e-af128cc9f59c>.
- Meirink, J. F., V. K. Makin, and V. N. Kudryavtsev, 2003: Note on the growth rate of water waves propagating at an arbitrary angle to the wind. *Bound.-Layer Meteor.*, **106**, 171–183, <https://doi.org/10.1023/A:1020835211837>.
- Mitsuyasu, H., and Y. Yoshida, 2005: Air–sea interactions under the existence of opposing swell. *J. Oceanogr.*, **61**, 141–154, <https://doi.org/10.1007/s10872-005-0027-1>.
- Moeng, C.-H., 1984: A large-eddy-simulation model for the study of planetary boundary-layer turbulence. *J. Atmos. Sci.*, **41**, 2052–2062, [https://doi.org/10.1175/1520-0469\(1984\)041<2052:ALESMF>2.0.CO;2](https://doi.org/10.1175/1520-0469(1984)041<2052:ALESMF>2.0.CO;2).
- , and P. Sullivan, 2015: Large eddy simulation. *Encyclopedia of Atmospheric Sciences*, Vol. 4, 2nd ed. G. North, F. Zhang, and J. Pyle, Eds., Academic Press, 232–240, <https://doi.org/10.1016/B978-0-12-382225-3.00201-2>.
- Moon, I.-J., I. Ginis, T. Hara, H. L. Tolman, C. W. Wright, and E. J. Walsh, 2003: Numerical simulation of sea surface directional wave spectra under hurricane wind forcing. *J. Phys. Oceanogr.*, **33**, 1680–1706, <https://doi.org/10.1175/2410.1>.
- , T. Hara, I. Ginis, S. E. Belcher, and H. L. Tolman, 2004: Effect of surface waves on air–sea momentum exchange. Part I: Effect of mature and growing seas. *J. Atmos. Sci.*, **61**, 2321–2333, [https://doi.org/10.1175/1520-0469\(2004\)061<2321:EOSWOA>2.0.CO;2](https://doi.org/10.1175/1520-0469(2004)061<2321:EOSWOA>2.0.CO;2).
- , J.-I. Kwon, J.-C. Lee, J.-S. Shim, S. K. Kang, I. S. Oh, and S. J. Kwon, 2009: Effect of the surface wind stress parameterization on the storm surge modeling. *Ocean Modell.*, **29**, 115–127, <https://doi.org/10.1016/j.oceomod.2009.03.006>.
- Mueller, J. A., and F. Veron, 2009: Nonlinear formulation of the bulk surface stress over breaking waves: Feedback mechanisms from air-flow separation. *Bound.-Layer Meteor.*, **130**, 117–134, <https://doi.org/10.1007/s10546-008-9334-6>.
- Peirson, W. L., and A. W. Garcia, 2008: On the wind-induced growth of slow water waves of finite steepness. *J. Fluid Mech.*, **608**, 243–274, <https://doi.org/10.1017/S002211200800205X>.
- , —, and S. E. Pells, 2003: Water wave attenuation due to opposing wind. *J. Fluid Mech.*, **487**, 345–365, <https://doi.org/10.1017/S0022112003004750>.
- Powell, M. D., P. J. Vickery, and T. A. Reinhold, 2003: Reduced drag coefficient for high wind speeds in tropical cyclones. *Nature*, **422**, 279–283, <https://doi.org/10.1038/nature01481>.
- Reichl, B. G., T. Hara, and I. Ginis, 2014: Sea state dependence of the wind stress over the ocean under hurricane winds. *J. Geophys. Res. Oceans*, **119**, 30–51, <https://doi.org/10.1002/2013JC009289>.
- Reul, N., H. Branger, and J.-P. Giovanangeli, 2008: Air flow structure over short-gravity breaking water waves. *Bound.-Layer Meteor.*, **126**, 477–505, <https://doi.org/10.1007/s10546-007-9240-3>.
- Richter, D. H., and P. P. Sullivan, 2013: Sea surface drag and the role of spray. *Geophys. Res. Lett.*, **40**, 656–660, <https://doi.org/10.1002/grl.50163>.
- Roekel, L. V., B. Fox-Kemper, P. P. Sullivan, P. E. Hamlington, and S. Haney, 2012: The form and orientation of Langmuir cells for misaligned winds and waves. *J. Geophys. Res.*, **117**, C05001, <https://doi.org/10.1029/2011JC007516>.
- Savelyev, I. B., M. P. Buckley, and B. K. Haus, 2020: The impact of nonbreaking waves on wind-driven ocean surface turbulence. *J. Geophys. Res. Oceans*, **125**, e2019JC015573, <https://doi.org/10.1029/2019JC015573>.
- Snyder, R. L., F. W. Dobson, J. A. Elliott, and R. B. Long, 1981: Array measurements of atmospheric pressure fluctuations above surface gravity waves. *J. Fluid Mech.*, **102**, 1–59, <https://doi.org/10.1017/S0022112081002528>.
- Sullivan, P. P., and J. C. McWilliams, 2010: Dynamics of winds and currents coupled to surface waves. *Annu. Rev. Fluid Mech.*, **42**, 19–42, <https://doi.org/10.1146/annurev-fluid-121108-145541>.
- , —, and C.-H. Moeng, 2000: Simulation of turbulent flow over idealized water waves. *J. Fluid Mech.*, **404**, 47–85, <https://doi.org/10.1017/S0022112099006965>.
- , —, and E. G. Patton, 2014: Large-eddy simulation of marine atmospheric boundary layers above a spectrum of moving waves. *J. Atmos. Sci.*, **71**, 4001–4027, <https://doi.org/10.1175/JAS-D-14-0095.1>.
- , M. L. Banner, R. P. Morison, and W. L. Peirson, 2018a: Impacts of wave age on turbulent flow and drag of steep waves. *Procedia IUTAM*, **26**, 174–183, <https://doi.org/10.1016/j.piutam.2018.03.017>.
- , —, —, and —, 2018b: Turbulent flow over steep steady and unsteady waves under strong wind forcing. *J. Phys. Oceanogr.*, **48**, 3–27, <https://doi.org/10.1175/JPO-D-17-0118.1>.
- Suzuki, N., Y. Toba, and S. Komori, 2010: Examination of drag coefficient with special reference to the wind sea Reynolds number: Conditions with counter and mixed swell. *J. Oceanogr.*, **66**, 731–739, <https://doi.org/10.1007/s10872-010-0060-6>.
- , T. Hara, and P. P. Sullivan, 2013: Impact of breaking wave form drag on near-surface turbulence and drag coefficient over young seas at high winds. *J. Phys. Oceanogr.*, **43**, 324–343, <https://doi.org/10.1175/JPO-D-12-0127.1>.
- Teixeira, M., 2018: A model for the wind-driven current in the wavy oceanic surface layer: Apparent friction velocity

- reduction and roughness length enhancement. *J. Phys. Oceanogr.*, **48**, 2721–2736, <https://doi.org/10.1175/JPO-D-18-0086.1>.
- Tolman, H. L., and D. Chalikov, 1996: Source terms in a third-generation wind wave model. *J. Phys. Oceanogr.*, **26**, 2497–2518, [https://doi.org/10.1175/1520-0485\(1996\)026<2497:STIATG>2.0.CO;2](https://doi.org/10.1175/1520-0485(1996)026<2497:STIATG>2.0.CO;2).
- Troitskaya, Y., D. Sergeev, O. Ermakova, and G. Balandina, 2011: Statistical parameters of the air turbulent boundary layer over steep water waves measured by the PIV technique. *J. Phys. Oceanogr.*, **41**, 1421–1454, <https://doi.org/10.1175/2011JPO4392.1>.
- , D. A. Sergeev, O. Druzhinin, A. A. Kandaurov, O. S. Ermakova, E. V. Ezhova, I. Esau, and S. Zilitinkevich, 2014: Atmospheric boundary layer over steep surface waves. *Ocean Dyn.*, **64**, 1153–1161, <https://doi.org/10.1007/s10236-014-0743-4>.
- Veron, F., 2015: Ocean spray. *Annu. Rev. Fluid Mech.*, **47**, 507–538, <https://doi.org/10.1146/annurev-fluid-010814-014651>.
- , G. Saxena, and S. K. Misra, 2007: Measurements of the viscous tangential stress in the airflow above wind waves. *Geophys. Res. Lett.*, **34**, L19603, <https://doi.org/10.1029/2007GL031242>.
- Wang, D., T. Kukulka, B. G. Reichl, T. Hara, and I. Ginis, 2019: Wind–wave misalignment effects on Langmuir turbulence in tropical cyclone conditions. *J. Phys. Oceanogr.*, **49**, 3109–3126, <https://doi.org/10.1175/JPO-D-19-0093.1>.
- Yang, D., and L. Shen, 2010: Direct-simulation-based study of turbulent flow over various waving boundaries. *J. Fluid Mech.*, **650**, 131–180, <https://doi.org/10.1017/S0022112009993557>.
- , and —, 2017: Direct numerical simulation of scalar transport in turbulent flows over progressive surface waves. *J. Fluid Mech.*, **819**, 58–103, <https://doi.org/10.1017/jfm.2017.164>.
- , C. Meneveau, and L. Shen, 2013: Dynamic modelling of sea-surface roughness for large-eddy simulation of wind over ocean wave field. *J. Fluid Mech.*, **726**, 62–99, <https://doi.org/10.1017/jfm.2013.215>.
- Yang, Z., B.-Q. Deng, and L. Shen, 2018: Direct numerical simulation of wind turbulence over breaking waves. *J. Fluid Mech.*, **850**, 120–155, <https://doi.org/10.1017/jfm.2018.466>.
- Young, I. R., and R. J. Sobey, 1985: Measurements of the wind-wave energy flux in an opposing wind. *J. Fluid Mech.*, **151**, 427–442, <https://doi.org/10.1017/S0022112085001033>.
- Yousefi, K., F. Veron, and M. P. Buckley, 2020: Momentum flux measurements in the airflow over wind-generated surface waves. *J. Fluid Mech.*, **895**, A15, <https://doi.org/10.1017/jfm.2020.276>.
- Zdyrski, T., and F. Feddersen, 2020: Wind-induced changes to surface gravity wave shape in deep to intermediate water. *J. Fluid Mech.*, **903**, A31, <https://doi.org/10.1017/jfm.2020.628>.